Jumping in frogs: assessing the design of the skeletal system by anatomically realistic modeling and forward dynamic simulation

William J. Kargo*, Frank Nelson† and Lawrence C. Rome‡

Department of Biology, University of Pennsylvania, Philadelphia, PA 19104, USA

*Present address: Neurosciences Institute, 10640 John Jay Hopkins Drive, San Diego, CA 92121, USA
†Present address: Department of Zoology, 3029 Cordley Hall, Oregon State University, Convallis, OR 97331-2914, USA
‡Author for correspondence (e-mail: lrome@sas.upenn.edu)

Summary

Comparative musculoskeletal modeling represents a tool to understand better how motor system parameters are fine-tuned for specific behaviors. Frog jumping is a behavior in which the physical properties of the body and musculotendon actuators may have evolved specifically to extend the limits of performance. Little is known about how the joints of the frog contribute to and limit jumping performance. To address these issues, we developed a skeletal model of the frog *Rana pipiens* that contained realistic bones, joints and body-segment properties. We performed forward dynamic simulations of jumping to determine the minimal number of joint degrees of freedom required to produce maximal-distance jumps and to produce jumps of varied take-off angles. The forward dynamics of the models was driven with joint torque patterns determined from inverse dynamic analysis of jumping in experimental frogs. When the joints were constrained to rotate in the extension–flexion plane, the simulations produced short jumps with a fixed angle of take-off. We found that, to produce maximal-distance jumping, the skeletal system of the frog must minimally include a gimbal joint at the hip (three rotational degrees of freedom), a universal Hooke's joint at the knee (two rotational degrees of freedom) and pin joints at the ankle, tarsometatarsal, metatarsophalangeal and iliosacral joints (one rotational degree of freedom). One of the knee degrees of freedom represented a unique kinematic mechanism (internal rotation about the long axis of the tibiofibula) and played a crucial role in bringing the feet under the body so that maximal jump distances could be attained. Finally, the out-of-plane degrees of freedom were found to be essential to enable the frog to alter the angle of take-off and thereby permit flexible neuromotor control. The results of this study form a foundation upon which additional model subsystems (e.g. musculotendon and neural) can be added to test the integrative action of the neuromusculoskeletal system during frog jumping.

Key words: frog, jumping, *Rana pipiens*, modelling, behaviour degrees of freedom, skeleton, joint, torque.

Introduction

Over the past two decades, there has been an intense effort to integrate information about muscle function at all levels of organization (Rome and Lindstedt, 1997, 1998). An ultimate goal of this integrative approach is to understand enough about the molecular and macroscopic components of muscular systems so that a comprehensive model can be developed that would enable us to predict how alterations in one parameter (e.g. crossbridge detachment rate) will affect motor performance.

With the recent development of new biophysical and whole-animal techniques, we are for the first time in the position where molecular properties can be related to whole-animal function in a quantitative manner. To proceed to this new level, it is important to have an animal and behavioral model in which (i) muscle length changes and the recruitment pattern of the responsible fiber types can be determined, (ii)

the overall body biomechanics are well defined and (iii) the molecular and biophysical properties of the fiber types are measurable.

The frog *Rana pipiens* presents a superb model in all these respects. Although different fiber types in frogs are not anatomically separated as in fish (Rome et al., 1984), the extensor muscles used for jumping are quite homogeneous in fiber type and mechanical properties (Lutz et al., 1998). In addition, there is compelling evidence that during maximal-distance jumping all the extensor muscle fibers are maximally activated (Hirano and Rome, 1984; Lutz and Rome, 1994, 1996a). Thus, the extensor muscles of a jumping frog behave similarly to an isolated muscle experiment in which the fiber (or bundle pure in fiber type) is maximally activated by direct electrical stimulation. This represents a tremendous simplification in terms of modeling. Further, frog muscle fibers

are amenable to all physiological and biophysical techniques. Finally, because of the large muscle strains compared with cyclical locomotory movements such as running and swimming, the muscle length changes and overall body mechanics during the one-shot ballistic jump of frogs can be relatively easily quantified (Calow and Alexander, 1973; Hirano and Rome, 1984; Marsh, 1994; Marsh and John-Alder, 1994; Peplowsiki and Marsh, 1997).

Still, a significant obstacle to integrating from muscle function to locomotion is that the musculoskeletal system of any animal is complex. Previously, we conducted experiments on the semimembranosous muscle of frog and tried to relate its mechanical performance to overall jumping performance (Lutz and Rome, 1994, 1996a,b). However, frog hindlimbs have in excess of 15 muscles that contribute to overall performance, and these muscles may perform different types of contraction (Mai and Lieber, 1990; Olson and Marsh, 1998; Gillis and Biewener, 2000). Thus, it is difficult to predict whole-animal movements from the mechanics of a single (or even a few) muscles. Musculoskeletal modeling can be an enormous help by keeping track of the forces generated by multiple muscles, so that the net action of all the muscles can be determined. In addition to muscle function, modeling can provide insight into how other physical components (e.g. joints, ligaments, bones and segment mass distributions) affect the transformation of neuromotor commands into limb and body motions (Crago, 2000; Dhaherlab et al., 2000; Pandy and Sasaki, 2001; Yeadon, 1990).

In this study, we developed a skeletal model of the frog that contained the bones, joints and segment masses and moments of inertia as a first step towards creating an integrative musculoskeletal model. In addition to measuring and describing the anatomical features of the frog skeleton, we used the model along with a reverse-engineering approach to test important aspects of the design and function of the skeletal system of frogs. Frog jumps differ from those of humans and other mammals in several important ways. In frogs, the hindlimb bones do not lie in a single plane throughout the jump, and hindlimb joint rotations other than extension are prominent (Lombard and Abbot, 1906; Gans and Parsons, 1966). Further, two joints (the tarsometatarsal and iliosacral), which are nearly fixed in humans, are flexible in proficient jumpers such as *Rana pipiens*, and they may contribute greatly to performance (Emerson and de Jongh, 1980).

We tested the importance of the extra joints and degrees of freedom using our model. We performed a series of forward dynamic simulations of jumping while varying the number of joints and degrees of freedom in different configurations of the model. We compared simulated jumping performance with the jumping performance of real frogs. Further, because the ability to alter the jumping trajectory may be important in the frog's behavioral repertoire, we also tested how these additional joints and degrees of freedom create opportunities to produce a wide range of jumping trajectories.

Materials and methods
Kinematic and inverse dynamic analyses of frog jumping

To obtain the joint torque information necessary to drive our forward-dynamic simulations and ultimately to compare the kinematics of virtual jumps with actual jumps, we needed first to analyze the three-dimensional kinematics of jumping frogs. High-speed cine film (200 frames s^{-1}) of jumping frogs by Lutz and Rome (1994, 1996a,b) was analyzed. The film contained orthogonal views of jumps (top and side views), and corrections were made, as detailed by Lutz and Rome (1996a), for parallax errors that occur with a 45° mirror. From the films, we determined the trajectory of the frog's center of mass (COM), which was located near the center of the abdominal-thoracic segment, the three-dimensional joint angles at the hip and knee and the one-dimensional joint angles (flexion–extension) about the iliosacral, ankle, tarsometatarsal and metatarsophalangeal joints (Fig. 1). We followed a procedure detailed by Vaughan et al. (1996) for calculating three-dimensional joint angles at the hip and knee. This procedure is detailed in Electronic Appendix 1. In short, three markers were digitized on the pelvis, thigh and calf segments. An orthogonal *x*, *y*, *z* reference system was embedded in each of these segments based on the locations of the markers. The angular orientation of the segments was determined in three-dimensional space, and the orientation of one segment was determined relative to another (e.g. the thigh relative to the pelvis and the calf relative to the thigh). Five jumps in three different frogs were examined in this way.

To find the torques produced during jumping (Fig. 1), we performed an inverse dynamic analysis. The joint velocities and accelerations were estimated using a difference equation in which the difference between data points was 5 ms (i.e. 200 frames s^{-1}). The time series of joint angles, joint velocities and joint accelerations were input to SIMM (Software for Interactive Musculoskeletal Modeling, Motion Analysis Corporation, Santa Rosa, CA, USA), which is a graphical modeling environment, together with the estimated inertial parameters of the frog body segments (e.g. center of mass location, mass and inertia tensor, see *Segmental inertial measurements*). Dynamics Pipeline Software (Motion Analysis Corporation, Santa Rosa, CA, USA) was then used to connect the SIMM motion file to SD/Fast (Symbolic Dynamics, Inc., Mountain View, CA, USA). The SD/Fast software then solved the following inverse dynamic equation for the system (in 1 ms time steps):

$$\mathbf{T}(\mathbf{q},\dot{\mathbf{q}}) = \ddot{\mathbf{q}}I - [\mathbf{G}(\mathbf{q}) + \mathbf{V}(\mathbf{q},\dot{\mathbf{q}})], \qquad (1)$$

where **q** is a vector of generalized coordinates, which includes three hip angles, three knee angles and flexion–extension angles at the ankle, tarsometatarsal and iliosacral joints (for kinematic descriptions, see *Establishment of local coordinate frames*), $\dot{\mathbf{q}}$ and $\ddot{\mathbf{q}}$ are the first and second derivatives, respectively, of **q**, $\mathbf{T}(\mathbf{q},\dot{\mathbf{q}})$ is the vector of joint torque inputs (due to muscle activation) that is driving joint motion, $\mathbf{G}(\mathbf{q})$ and $\mathbf{V}(\mathbf{q},\dot{\mathbf{q}})$ are vectors of gravity- and motion-dependent terms and *I* is the system mass matrix. SD/Fast used Kane's method
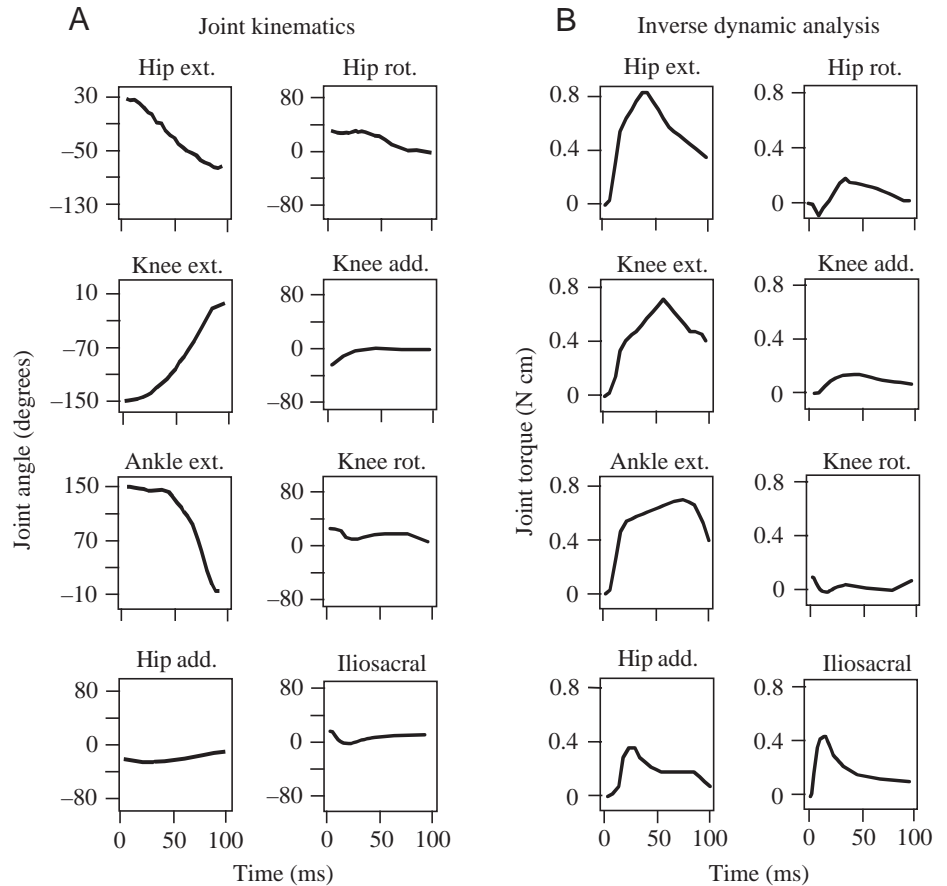
Fig. 1. Joint kinematics (A) and joint torque patterns (B) during a maximal-effort jump in *Rana pipiens*. (A) The joint angle changes during the take-off phase of jumping (when the feet are in contact with the ground) are shown. In each panel, the *y* axis (joint angle) has the same range of 160°. (B) The net torques due to the combination of active muscle forces, passive forces in connective tissues and forces arising from interaction between the metatarsal segment and the ground (see Materials and methods). In each panel, the *y* axis (torque) has a range of 0.8 N cm. The joint degrees of freedom (DOFs) illustrated are: extensor DOF of the hip (Hip ext.), extensor DOF of the knee (Knee ext.), extensor DOF of the ankle (Ankle ext.), adduction DOF of the hip (Hip add.), external rotation DOF of the hip (Hip rot.), adduction DOF of the knee (Knee add.), external rotation DOF of the knee (Knee rot.) and the iliosacral joint.

to compute $\mathbf{T}(\mathbf{q},\dot{\mathbf{q}})$ required to produce the body-segment rotations measured from kinematic analyses. In performing these calculations, the metatarsal segment was assumed to be rigidly fixed to the ground to avoid having to supply the ground reaction forces to the inverse dynamics solver. Joint torque values were computed for a total of five jumps by three different frogs.

Bone scanning

The bones of the frog *Rana pipiens* (Schreber) were scanned using a three-dimensional laser scanner (resolution 50 μm) manufactured by Cyberware (Cyberware Inc., Monterey, CA, USA) and controlled by a Silicon Graphics O$_2$ UNIX computer. An average-sized frog, 28 g mass and with an extended hindlimb length of approximately 90 mm, was killed with an overdose of Tricaine (Sigma Chemical Co.) and pithed in accordance with IACUC procedures. Excess muscle, organs and connective tissues were dissected from the skeleton, but all tissues surrounding the joints were left intact to ensure proper joint motion. The intact skeleton of the frog was placed on a rotating stage, and the scanner was initiated to move in the horizontal direction to obtain one surface scan of the skeleton. The stage was rotated by 10°, and a second surface scan of the skeleton was taken. The skeleton was scanned and rotated 36 times (i.e. in 10° increments) to obtain a complete three-dimensional scan. The skeleton was then placed on the rotating stage in a different orientation and a second three-

dimensional scan was obtained. This was performed five times to obtain five complete scans. The scans were merged into a single three-dimensional image of the skeleton using software from Cyberware. Individual bone segments were then disarticulated, and the remaining skeletal complex was scanned using the above procedure. All the removed bone segments were individually scanned as well. This procedure was used so that the relative positioning between bone segments was maintained in the graphical modeling environment (see below). For example, the femur and tibiofibula, which are connected at the knee joint, were scanned together with connective tissues intact and then individually scanned after disarticulating the two bones. The individual scans were then correctly positioned relative to each other by matching their orientations to an overlaid scan of the entire bone complex.

The three-dimensional images of the individual bone segments were converted into bone files by a utility program in SIMM 2.2. The bone files, which list the polygons and polygon coordinates that compose the three-dimensional image, were then imported into SIMM, where the correct orientation between bones was maintained.

Establishment of local coordinate frames

In SIMM, the individual bone segments were positioned in a configuration that served as an arbitrary starting point or reference anatomical position. In this configuration, all the bones rested in a horizontal plane (see Fig. 2). A local

coordinate frame was attached to the following bone segments: femur, tibiofibula, astragalus–calcaneus segment, metatarsophalangeal segment, pelvis, urostyle, vertebral column (all nine vertebrae considered as a single rigid segment) and skull.

The orientation and the origin of the local coordinate frames (LCFs) were established as follows. The pelvis LCF was oriented such that the x axis pointed from the central acetabulum of the right hip joint through the central acetabulum of the left hip joint. The z axis was orthogonal to the x axis and pointed dorsally in the reference configuration (i.e. out of the page when looking down on the frog). The y axis was determined by the right-hand rule and pointed caudally along the long axis of the pelvis. The origin of the pelvis LCF was positioned mid-way between the centers of the right and left acetabula.

The LCF for both the right and left femora was oriented such that the x axis was parallel to the long axis of the femur and pointed to the frog's left when in the reference position. The z axis was orthogonal to the x axis and pointed dorsally in the reference position. The femur y axis was determined by the right-hand rule and pointed caudally in the reference position. The origin of the femur LCF was positioned at the instantaneous center of femoral rotation relative to the pelvis (see *Joint kinematics: descriptions, measurements and modeling*). This position was located approximately 1.5 mm from the most central, proximal point of the femur and within the femoral head. The LCFs for the tibiofibula, astragalus–calcaneus and metatarsophalangeal segments were oriented in a manner similar to that of the femur LCF, i.e. the x axis for each LCF was parallel to the long axis of the bone segment, the z axis pointed dorsally in the reference configuration and the y axis was determined by the right-hand rule. The origin of each of these segments' LCFs was positioned to intersect with the most proximal, central point of the respective bone segment.

The origin of the vertebral segment's LCF was positioned at the most caudal, central tip of the sacrum. The sacrum is the most caudal vertebra next to the elongated urostyle, and its transverse processes form a joint with the most rostral tips of the iliac crest (Emerson and de Jongh, 1980). In the reference configuration, the z axis of the vertebral segment pointed dorsally, the x axis pointed to the left of the frog and the y axis pointed caudally. The origin of the skull's LCF was positioned at a central point within the foramen magnum at the level of the skull's attachment to the first vertebra. The axes were oriented similarly to that of the vertebral segment's axes. Finally, the origin of the urostyle's LCF was positioned at the most rostral, central tip of the urostyle, where it articulated with the sacrum. In this report, we do not discuss LCFs for the forelimb bones and for the clavicle–scapula–sternum segment.

Joint kinematics: descriptions, measurements and modeling

A joint specifies the displacements that relate the position and orientation of a moving bone segment relative to a reference or fixed bone segment. In the frog model, the following joints were defined: hip joints, displacement of the femur relative to the pelvis; knee joints, displacement of the tibiofibula relative to the femur; ankle joints, displacement of the astragalus–calcaneus segment relative to the tibiofibula; tarsometatarsal joints, displacement of the metatarsophalangeal segment relative to the astragalus segment; iliosacral joint, displacement of the vertebral segment relative to the pelvis; and sacro-urostyle joint, displacement of the urostyle relative to the vertebral segment. The forelimb joints were ignored, and the joint between the first vertebra and skull was fixed such that the angle between their respective y axes was $0°$.

We used a custom-made jig apparatus (see Lutz and Rome, 1996a) to measure the kinematics of a moving joint member with respect to a fixed joint member. For each joint examined, the fixed and mobile bone segments were removed from frogs as a single unit. Major limb muscles were removed from the bone segments, but small muscles, ligaments and other connective tissues surrounding the joint capsule were left intact. The fixed and mobile members were rigidly secured to the stationary and moving arms of the jig, respectively, by Mizzy low-heat compound. For the hip, the pelvis was fixed and the femur was mobile. For the knee, the femur was fixed and the tibiofibula was mobile. For the ankle, the tibiofibula was fixed and the astragalus–calcaneus segment was mobile. For the tarsometatarsal joint, the astragalus was fixed and the metatarsal segment was mobile. For the iliosacral joint, the pelvis was fixed and the vertebral column was mobile. The jig permitted $180°$ of rotation and unopposed translation of the mobile member relative to the fixed member within a single plane of motion. A digital camera (Nikon Coolpix 990, 1.8 megapixels) was positioned orthogonal to this plane of motion, 1.83 m from the approximate center of the joint. The horizontal and vertical dimensions of the digital image were calibrated by placing rulers in the view of the camera along both dimensions.

The joint members were placed in the reference position in the jig (reference position shown in Fig. 2), and the mobile member was first rotated about its z axis. Rotation about the z axis is the primary range of motion in the frog hindlimb joints and was referred to here as flexion–extension. The top row of Fig. 3 shows the flexion–extension ranges of motion for the hip, knee, ankle and tarsometatarsal joints. Counterclockwise rotation of the left femur about its z axis was termed hip extension and clockwise rotation was termed hip flexion (opposite convention for the right hip). Counterclockwise rotation of the left tibiofibula was termed knee flexion and clockwise rotation was termed knee extension (opposite for the right knee). Counterclockwise rotation of the left astragalus segment about its z axis was termed ankle extension and clockwise rotation was termed ankle flexion (opposite for the right ankle). The flexion–extension angle for each joint was the angle between the x axis of the moving segment and the x axis of the fixed segment (dotted line in top row of Fig. 3). Each hindlimb joint was rotated through a $160°$ range of flexion–extension, and a digital image was captured at each $10°$ increment.
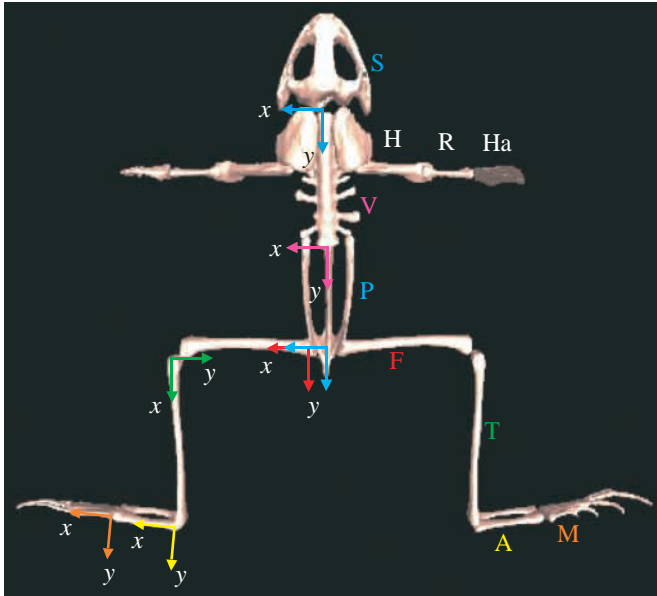
Fig. 2. The bone segments (right) of *Rana pipiens* and the local coordinate frames (LCFs) (left) attached to each bone segment in SIMM software. The bone segments are positioned in the 'reference position', a position in which all the bones rest in a single, horizontal plane. In the reference position, the *z* axis of the LCF points out of the page. The orientation of the *x* and *y* axes for each segment are shown with different colors (orange, metatarsophalangeals, M; yellow, astragalus–calcaneus, A; green, tibiofibula, T; red, femur, F; light blue, pelvis, P; purple, vertebral column, V; dark blue, skull, S). The LCF for the urostyle overlaps that of V and is not shown. The LCFs for the forelimb bones (humerus, H; radius, R; hand, Ha) are not shown.

After measuring flexion–extension kinematics at the hindlimb joints, the joint members were re-positioned in the jig and placed in the reference configuration. The moving member was then rotated about its *y* axis. Rotation about the *y* axis of a hindlimb bone was referred to here as abduction–adduction. The second row of Fig. 3 shows the abduction–adduction ranges for the hip and knee. The ankle and tarsometatarsal joints had small (<20°) ranges of abduction–adduction and are not shown. Counterclockwise rotation of the left femur and tibiofibula about the respective *y* axes was termed adduction and clockwise rotation was termed abduction (opposite convention for the right hindlimb). The abduction angle was the angle between the *z* axis of the moving member in the reference position (dotted line in the second row of Fig. 3) and the *z'*-axis in the rotated position. The femur was rotated through an abduction–adduction range of 120°, and the tibiofibula was rotated through a range of 60°, each in 10° increments.

After measuring abduction–adduction kinematics at the hindlimb joints, the joint members were re-positioned in the jig and placed in the reference configuration. The moving member was then rotated about its long axis (*x* axis) using the jig's second, independent axis of rotation. Rotation about the long axis of a hindlimb bone is referred to here as

external–internal rotation. The third row of Fig. 3 shows the external–internal ranges of motion for the hip and knee. The ankle and tarsometatarsal joints had small (<15°) ranges of external–internal rotation and so are not shown. When viewed proximally to distally down the shaft of the moving bone (as in Fig. 3), counterclockwise rotation about the long axis was termed internal rotation and clockwise rotation was termed external rotation. The external–internal rotation angle was the angle between the *y* axis of the moving segment in the reference position (dotted line in third row of Fig. 3) and the *y'*-axis in its rotated position. The femur was rotated through a range of 100°, and the tibiofibula was rotated through a range of 60°, each in 10° increments.

To measure the kinematics of the iliosacral joint, the pelvis was secured to the fixed arm of the jig and the vertebral column was secured to the moving arm. The vertebral column was rotated through a 100° range of motion about its *x* axis, and images were captured every 10°. When viewed from the frog's right side (as in the lower right panel of Fig. 3), counterclockwise rotation of the vertebral segment was termed vertebral extension and clockwise rotation was termed flexion. Rotations about the other axes of the vertebral segment are minimal in the frog (Emerson and de Jongh, 1980), so these were not measured. Iliosacral joint images were captured in four frogs, hip joint images in eight frogs, knee images in six frogs and ankle images in five frogs.

The images were analyzed to determine the locations of the instantaneous centers of rotation about each joint axis examined (see Lieber and Boakes, 1988). To minimize the errors associated with determining the instantaneous center of rotation, extended wires (4 cm in length) were placed into the moving segment before the joint images were captured. One wire was placed along the long axis of the bone and a second wire was placed perpendicular to the long axis. Markers (1 mm²) were then placed at the tips of each wire. The marker positions (*A* and *B*) at each successive joint position were digitized in Matlab. The location of the instantaneous center of rotation was determined to be the intersection point of the perpendicular bisectors of vector $\mathbf{A_nA_{n+1}}$ and vector $\mathbf{B_nB_{n+1}}$, where *n* refers to the position number and *n*+1 is the position resulting from a 10° rotation (Kinzel and Gutkowski, 1983).

The joint images were analyzed to determine the locations of the LCFs for the fixed and moving segments. The origins of the LCFs were marked on both segments using small dots of paint (approximately 0.50 mm²). The dot locations were digitized at successive rotation angles (10° increments). The location of the moving segment's origin was subtracted from the location of the fixed segment's origin at each rotation angle. Thus, for each joint axis, the *x* and *y* locations of the moving segment's LCF relative to the fixed segment's LCF were described as a function of the rotation angle θ. This information was used to model the appropriate kinematic functions in SIMM. In SIMM, three kinematic functions were specified for each joint, one for each joint axis. So, for example, translation between the femur and pelvis in the plane of hip extension was specified as a function of the hip extension
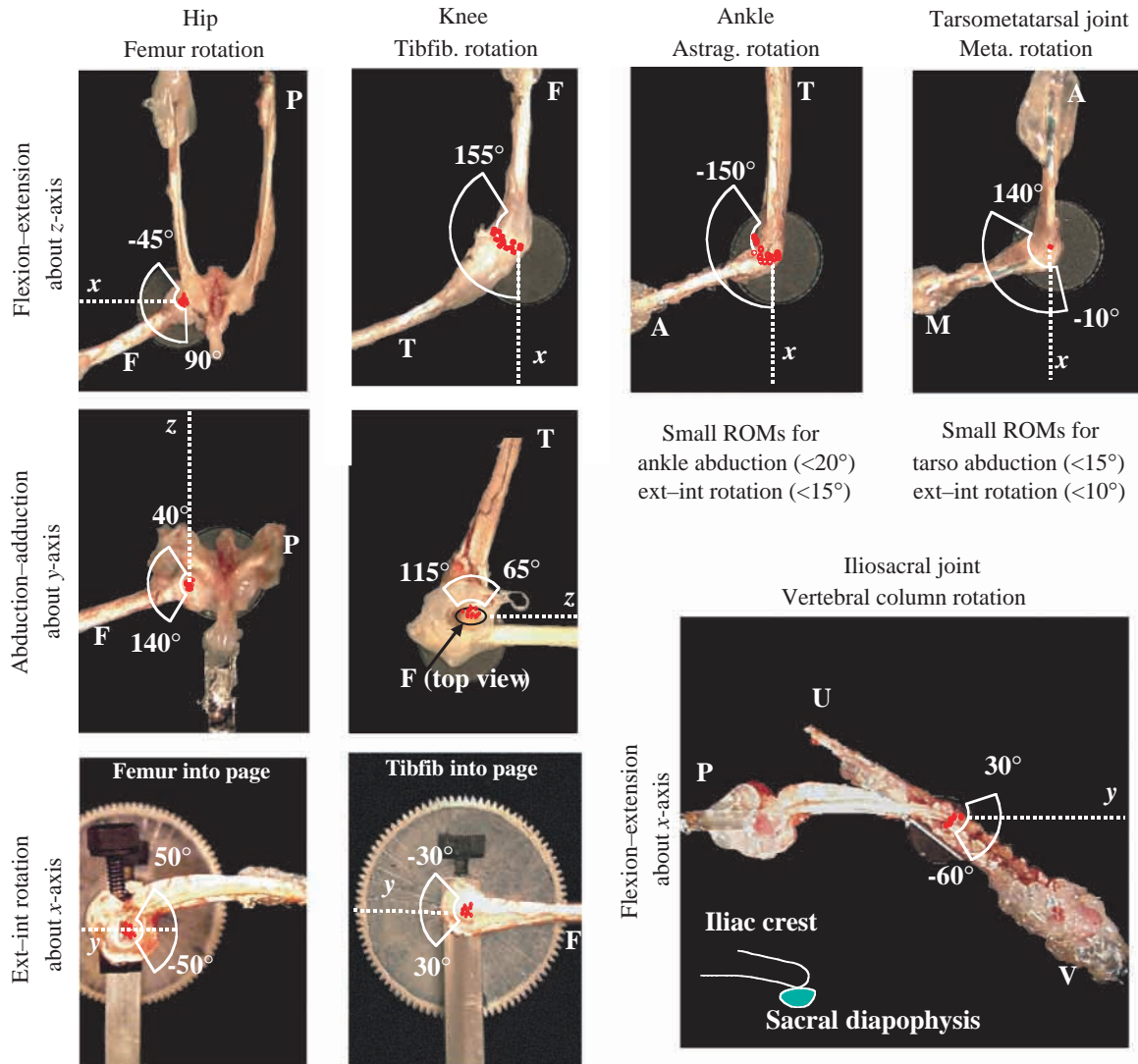
Fig. 3. The ranges of motion and passive kinematics for the hindlimb and iliosacral joints of *Rana pipiens*. The location of the instantaneous center of rotation was determined about each joint axis. The white arcs overlying the joint images represent the range of motion about each joint axis. Red dots represent the locations of the instantaneous centers of rotation measured over this range of motion. The dotted lines show the *x*, *y* and *z* axis. The left column shows the ranges of motion and kinematics for the hip joint: top panel, flexion–extension of the femur F relative to the pelvis P; middle panel, abduction–adduction of the femur; bottom panel, external–internal rotation of the femur. The hip kinematics corresponded most closely to the kinematics of a ball-and-socket joint. The second column shows the ranges of motion and kinematics for the knee joint: flexion–extension of the tibiofibula T relative to the femur, abduction–adduction of the tibiofibula and external–internal rotation of the tibiofibula (Tibfib). Flexion–extension kinematics at the knee corresponded most closely to the kinematics of a rolling joint, while the kinematics about the other axes corresponded more closely to the kinematics typical of hinge joints. The top panels of the third and fourth columns show the ranges of motion and kinematics for ankle flexion–extension (rotation of the astragalus segment A relative to tibiofibula), and tarsometatarsal flexion–extension (rotation of the metatarsals M relative to the tarsals). The ranges of motion (ROMs) about the other axes of these two joints were minimal (<20°). Flexion–extension kinematics at the ankle corresponded most closely to the kinematics of a rolling joint. Tarsometatarsal kinematics was represented in the model as a hinge joint (i.e. a single instantaneous center of rotation throughout the range of motion). The bottom right panel shows the ranges of motion and kinematics for the iliosacral joint (flexion–extension of the vertebral column V relative to the pelvis; U, urostyle). The kinematics at this joint corresponded most closely to a gliding joint. The inset shows a diagram of the sacral diaphysis, which is the transverse process of the sacrum that forms a joint with the iliac process of the pelvis.

angle. SIMM smoothly interpolates between the discretely specified variables using a natural cubic spline.

For three-dimensional rotations, the order of rotations about the specified axes is important and must be specified for a unique description of joint motion, i.e. the rotations are not commutative (Kinzel and Gutkowski, 1983). In our joint definitions, we specified the order of rotations to be rotation about the *z* axis, *x* axis and then *y* axis of the proximal

segment's LCF. Rotation about the *z* axis, i.e. flexion–extension, is the primary range of motion in the hindlimb, so this was chosen as the first rotational component in each joint. We found that changing the order of rotations had no discernible effect on the dynamic behavior of frog models examined (see *Forward dynamic modeling*).

Segmental inertial measurements

The mass, moment of inertia and center of mass were determined for each of the hindlimb and trunk segments. These measurements were then entered into a segment description file for inputting to SIMM. The segment mass and moments of inertia were determined in four frogs that had similar segment lengths (an extended hindlimb length of approximately 90 mm, see Table 1) and total mass (28 g) to the frog that was laser-scanned. Each frog was killed and frozen in the reference position. The body was cut into a number of segments; care was taken to make the cuts at similar positions and orientations in each frog. The segments included the thigh, calf, astragalus, foot (both metatarsals and phalanges included), a pelvic segment, which spanned from the most caudal aspect of the pelvis (ischium) to the most rostral tip of the iliac crest, an abdominal-thoracic (trunk) segment, which spanned from the tip of the iliac crest to the base of the skull, and the skull (see Fig. 4). These segments contained muscle, skin, tendon, organs and bone. Because these tissues have slightly different densities, an average density was measured for each segment. To do this, each segment was weighed to determine its mass (*M*) and then lowered into a water-filled graduated cylinder and its volume (*v*) was determined by weighing displaced water. The average density (ρ) was then calculated as described in Nigg (1999) as:

$$\rho = \frac{M}{v}. \qquad (2)$$

The moments of inertia for each segment were calculated as described by Yeadon (1990) based on a simplifying assumption that segment density was uniform and equal to the averaged density. Each segment was represented as a geometric solid of uniform density. We modeled the thigh, calf, pelvic, abdominal-thoracic and skull segments as stadium solids (see Yeadon, 1990). A stadium solid is an elongated geometric solid bounded by parallel stadia (i.e. a rectangle with an adjoining semicircle at each end of its width) on its two ends. The stadium dimensions were estimated by measuring several parameters of the frog segments. These parameters included the perimeter, width and depth of the segment ends (i.e. the bounding stadia) and the segment length (i.e. distance between the stadia). The astragalus segment was modeled as a cylinder, the foot segment was modeled as a cone and the specific dimensions for each were measured (see Electronic Appendix 2 for calculation of moments of inertia for each segment).

Forward dynamic modeling

In this study, we used forward dynamic simulations to test how different degrees of freedom in the hindlimb joints of the frog affect jumping performance. Forward dynamic simulations were performed using the Dynamics Pipeline software, which works by connecting the skeletal model in SIMM to SD/Fast. SD/Fast computes and solves the equations of motion for the model when given a set of forces or torques acting on the skeletal system. A separate equation of motion is solved for each degree of freedom and is of the general form described for other rigid-body, musculoskeletal models (Crago, 2000; Zajac, 1993):

$$\ddot{\mathbf{q}} = \mathbf{I}^{-1}[\mathbf{G}(\mathbf{q}) + \mathbf{V}(\mathbf{q},\dot{\mathbf{q}}) + \mathbf{T_M}(\mathbf{q},\dot{\mathbf{q}}) + \mathbf{T_P}(\mathbf{q},\dot{\mathbf{q}}) + \mathbf{T_E}(\mathbf{q},\dot{\mathbf{q}})], \qquad (3)$$

where variables are defined as previously described (see equation 1) and $\mathbf{I}^{-1}$ is the inverse mass matrix, $\mathbf{T_M}(\mathbf{q},\dot{\mathbf{q}})$ is the vector of joint moments due to muscle forces, $\mathbf{T_P}(\mathbf{q},\dot{\mathbf{q}})$ is a vector of passive moments due to stretching of connective tissues about the joints and $\mathbf{T_E}(\mathbf{q},\dot{\mathbf{q}})$ is a vector of moments that arise from interactions with the environment. In this study, we excluded submodels of the muscles and neural control to focus solely on the joint degrees of freedom that are critical for jumping performance. Therefore, to drive the motion of the model, we specified a pattern of joint torque inputs instead of specifying a muscle activation pattern. Thus, $\mathbf{T_M}(\mathbf{q},\dot{\mathbf{q}})$ from equation 3 was replaced with user-defined pattern of torque inputs, $\mathbf{T_I}$. In addition to simplifying the control input, we assumed the contributions of passive structures $\mathbf{T_P}(\mathbf{q},\dot{\mathbf{q}})$ to be negligible, so this term was removed from equation 3.

A series of progressively higher-dimensional models was constructed in which a kinematic degree of freedom (DOF) that was constrained in one model was relaxed in a subsequent model. The four models are described in the Results and shown schematically in Fig. 5. We used two strategies to examine the dynamic behavior of the frog models. In the first strategy, we wanted to explore the range of dynamic behaviors that the model was capable of producing. To do this, we applied unit torque steps about each relaxed, rotational DOF in the model to drive its motion. The torque steps were 80 ms in duration and applied synchronously about each joint. A vector of random numbers was generated before each simulation run to scale the magnitude of the applied torque steps. The scalars ranged from 0 to 0.009 N m for the hip extensor torque, from –0.004 to 0.004 N m for the hip external (–) or internal (+) rotation torque, from –0.004 to 0.004 N m for the hip adduction (–) or abduction (+) torque, from 0 to 0.007 N m for the knee extensor torque and from 0 to 0.007 N m for the ankle extensor torque. We set the maximum value for the extensor scalars (i.e. hip, knee and ankle extensor torques) to be the peak torque that the real frog produces during a representative, maximal-distance jump (see *Kinematics and inverse dynamic analyses of frog jumping*). For the other scalars, we chose an intermediate range of values in which both directions of torque (e.g. hip abduction and hip adduction) could be produced. For each model, 1000 simulations was run with different randomized scaling factors. We determined the trajectory of the COM, the take-off angle and the joint angles for each simulation run.

The second strategy to examine the dynamic behavior of the

frog models was simply to use the torque values produced by the real frog to drive the motion of the models. If we could not produce a maximal-distance jump in the model under study, then clearly something was lacking in the model.

Several assumptions were made in all the jumping simulations. In models 1–3, the right and left foot segments (metatarsals and phalanges) were fixed to the ground. In model 4, only the phalanges were fixed to the ground. By modeling the foot–ground contact as a jointed connection, ground reaction forces were automatically included in the model rather than having to supply them explicitly (Nigg, 1999). However, because each frog model was connected to the ground, jumping distance had to be estimated. Jump distance was calculated as the sum of the horizontal displacement of the COM during the take-off and aerial phases of the jump. The horizontal displacement during the aerial phase was estimated using ballistics equations described by Hirano and Rome (1984).

A second assumption we made in each simulation was that the forelimb segments could be removed without any effect on jumping performance. The forelimb segments are not likely to contribute much, if any, power to the jump (Calow and Alexander, 1973; Hirano and Rome, 1984; Peters et al., 1996; Marsh, 1994). Also, the small mass of the forelimb segments (approximately 5% of total body mass) is likely to have a negligible effect on the trajectory of the center of mass. We also assumed that the atlanto-occipital joint and intervertebral joints did not contribute significantly to jumping, and these joints were therefore held rigid in each model. Finally, we assumed that the iliosacral joint was a revolute joint in each model. The digitized measurements provide evidence that this joint may be a gliding joint, in which trunk translation and rotation are independent of one another (see *Behavior and modeling of the ankle, tarsometatarsal, metatarsophalangeal and iliosacral joints* in Results). However, gliding joints are computationally difficult to model, and others have hypothesized that translation of the trunk (relative to the pelvis) may be important only during swimming and in frogs specialized for swimming (Emerson and de Jongh, 1980).

Static analysis of force transmission

Measurements of the ground reaction force (GRF) can be used to predict the trajectory of the frog's COM using relatively simple ballistics equations (Hirano and Rome, 1984; Marsh, 1994). It is unclear whether and how the frog actively varies the GRF to generate different trajectories and take-off angles. If the goal is to produce a maximal-distance jump, the frog should generate GRFs that are oriented at approximately 42° to the ground (Hirano and Rome, 1984). However, if the goal is to jump over an obstacle or to generate low take-off angles (i.e. high accelerations), the frog must adjust the GRF to higher or lower angles, respectively. The degrees of freedom in the hindlimb models and the associated starting configuration might limit this ability. To examine the range of force directions that each model can produce, we calculated the Jacobian matrix for each model in its starting configuration, which was determined from video analysis of jumping frogs

(see *Kinematic and inverse dynamic analyses of jumping frogs*). The transpose of the Jacobian matrix relates the joint torques to the GRF by the following:

$$\tau = \mathbf{J^T F}, \qquad (4)$$

where τ is an *n*-dimensional joint torque vector, $\mathbf{F}$ is an *m*-dimensional end-effector output force and $\mathbf{J^T}$ is the transpose of the Jacobian matrix. $\mathbf{J}$ is an $m{\times}n$ matrix, where m denotes the degrees of freedom of the end-effector space and n denotes the number of actuated joint variables (calculation of $\mathbf{J}$ is shown in Electronic Appendix 3). For each of the models, the GRF during simulation runs was calculated at the starting configuration of the limb. The velocity and joint angles of the ensuing, dynamic jumps were then calculated. The GRFs at the starting limb configuration were related to the trajectory of the frog models using linear regression techniques.

Sensitivity analysis

We examined how sensitive jumping performance was to variations in the magnitude of individual joint torques. The torque pattern that was estimated using an inverse dynamic analysis of jumping was systematically modified by scaling the magnitude of each torque (e.g. the hip extensor torque) to 80–120% of its base value. Each torque component was individually examined in this way, including the iliosacral extensor torque. The sensitivity S_P of the vertical and horizontal velocities of the COM and the sensitivity of take-off angles in response to a change in the torque magnitude about a single axis was determined as:

$$S_P = [(\Delta V/V)/(\Delta T/T)], \qquad (5)$$

where V is a variable describing the trajectory (e.g. peak vertical velocity, horizontal velocity or take-off angle) and T is the joint torque, which is varied during the batch of simulations.

Results

Kinematic and inverse dynamic analyses of jumping frogs

The hindlimb and iliosacral joint kinematics were determined for five jumps in three different frogs (mean peak take-off velocity $1.7{\pm}0.08\,\mathrm{m\,s^{-1}}$, mean ± S.E.M.). Fig. 1A shows the joint kinematics during a maximal-effort jump in one frog. The peak take-off velocity of the COM during this jump was $1.95\,\mathrm{m\,s^{-1}}$, which occurred approximately 80 ms into the jump. The time course and range of hip, knee, ankle and iliosacral extension were similar to previously published values (Calow and Alexander, 1973; Lutz and Rome, 1996a; Peters et al., 1996). In addition, we found that flexion occurred about the tarsometatarsal joint for the first 60 ms and extension occurred about this joint for the last 15–20 ms. We also found some degree of rotation about the secondary degrees of freedom at the hip and knee joints. For the jump shown in Fig. 1A, there was a moderate amount of external rotation (range 30°) and abduction (range 25°) about the hip joint. These joint motions acted to bring the femur into the same plane as the long axis of

Table 1. *Body-segment properties of* Rana pipiens

Segment	Length (mm)	Proximal Width (mm)	Proximal Depth (mm)	Distal Width (mm)	Distal Depth (mm)	Mass (g)	Volume (cm³)	ρ (g cm⁻³)	I_x (g cm²)	I_y (g cm²)	I_z (g cm²)
Pelvis	23.1	14.9	12.1	10.1	10.9	3.6	3.3	1.1	2.5	3.1	4.2
Femur	26.8	15.1	10.1	7.3	5.5	2	1.8	1.1	0.6	1.9	2.3
Tibiofibula	30.7	7.3	4.9	5	4.8	1.4	1.2	1.2	0.2	1.2	1.4
Astrag.	15.4	4.9	4.9	4.9	4.9	0.4	0.4	1	0.1	0.8	0.8
Foot	28	4.9	4.9	4.9	4.9	0.5	0.5	1.1	0.1	0.2	0.2
Skull	19.2	25.1	16.2	5	3.1	3.8	3.8	1	1.8	1.6	1.7
Trunk-spine	20.2	25.2	17.4	18.1	12.1	10.3	9.4	1.1	5.3	4.7	7.2

The body was divided into 11 rigid-body segments (see Materials and methods): skull, trunk-spine, pelvis, two femoral, two tibiofibular, two astragalus–calcaneus (Astrag.) and two foot (metatarsals plus phalanges) segments. Segment length, the surface dimensions of the proximal and distal segment ends, mass, volume, density (ρ) and moments of inertia about the segment axes (I_x, I_y and I_z) were determined for each segment. Each value represents the mean of 4 frogs.

the pelvis. We also found moderate degrees of internal rotation (range 30°) and abduction (range 20°) about the knee joint. These joint motions acted similarly to bring the tibiofibula into the same plane as the femur and long axis of the pelvis.

On the basis of the kinematics of the analyzed jumps and the measured inertial parameters of the hindlimb and axial segments (Table 1), we estimated the net torques produced about each of the degrees of freedom during jumping. We used an inverse dynamic analysis and assumed the metatarsal segment to be rigidly fixed to the ground (see Materials and methods). The net torques about the iliosacral, hip, knee and ankle joints, which correspond to the jump shown in Fig. 1A, are presented in Fig. 1B. Net torques at each joint varied with time. Extensor torques about the iliosacral, hip, knee and ankle joints peaked at successively later times into the jump (15, 40, 50 and 70 ms, respectively) and this temporal staggering was consistent for each jump analyzed. The peak magnitude of the extensor torque was larger about the hip than about the knee and ankle joints (0.85±0.02 N cm, 0.7±0.04 N cm and 0.7±0.04 N cm, respectively; means ± S.E.M., *N*=5 jumps) and relatively smaller about secondary degrees of freedom at the hip and knee. For some jumps (data not shown), hip adduction torques were more significant (e.g. peak of 0.65 N cm; peak magnitude 0.4±0.05 N cm, mean ± S.E.M., *N*=5 jumps). The finding that extension ranges of motion and extensor torques were larger than motion and torques about the other degrees of freedom indicates that most of the joint work was performed by hip, knee and ankle extension.

Bones and segment properties of Rana pipiens

The bone segments that were laser-scanned and used to construct the skeletal models of *Rana pipiens* are shown in Fig. 2. The mass, moment of inertia, center of mass and geometric dimensions were determined for each of the hindlimb and trunk segments (Fig. 4), and the mean values from 4 frogs are shown in Table 1.

Behavior and model of the hip joint

A goal of this study was to determine the importance of joint

degrees of freedom to jumping performance. It was first necessary to measure the behavior and degrees of freedom of each joint in the real frog and then use this information to model the appropriate behavior of the virtual joints.

Flexion–extension is the primary range of motion at the hindlimb joints and represents rotation of a bone segment about the *z* axis of its LCF. The locations of the instantaneous centers of rotation for each joint during flexion–extension are shown as a collection of red dots in the top row of Fig. 3. The instantaneous centers of hip extension tended to cluster into a single, circumscribed region (area 1.6±0.19 mm², mean ± S.E.M., *N*=8) located within the femoral head and approximately 1.5 mm from its most proximal point. This tight clustering indicated that the location of the instantaneous center was approximately constant throughout the range of
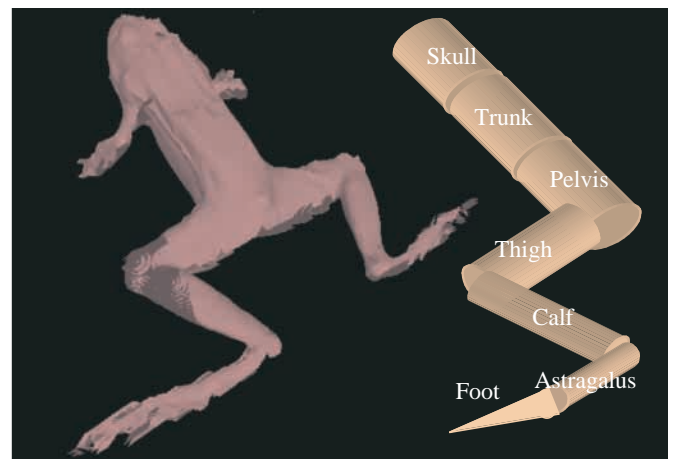

Fig. 4. The body segments of the frog were modeled as geometric primitives of uniform density. To the left is a scanned image of the whole frog body. To the right are the geometric solids used to approximate the inertial properties of the skull, trunk, pelvis, thigh and calf segments (stadium solids; see Materials and methods), the astragalus segment (cylinder) and the foot segment (cone). The dimensions, mass, averaged density and estimated inertias for each segment are shown in Table 1.

Model 1: planar hindlimb (5 DOFs)

Model 2: 3-D hip (7 DOFs)

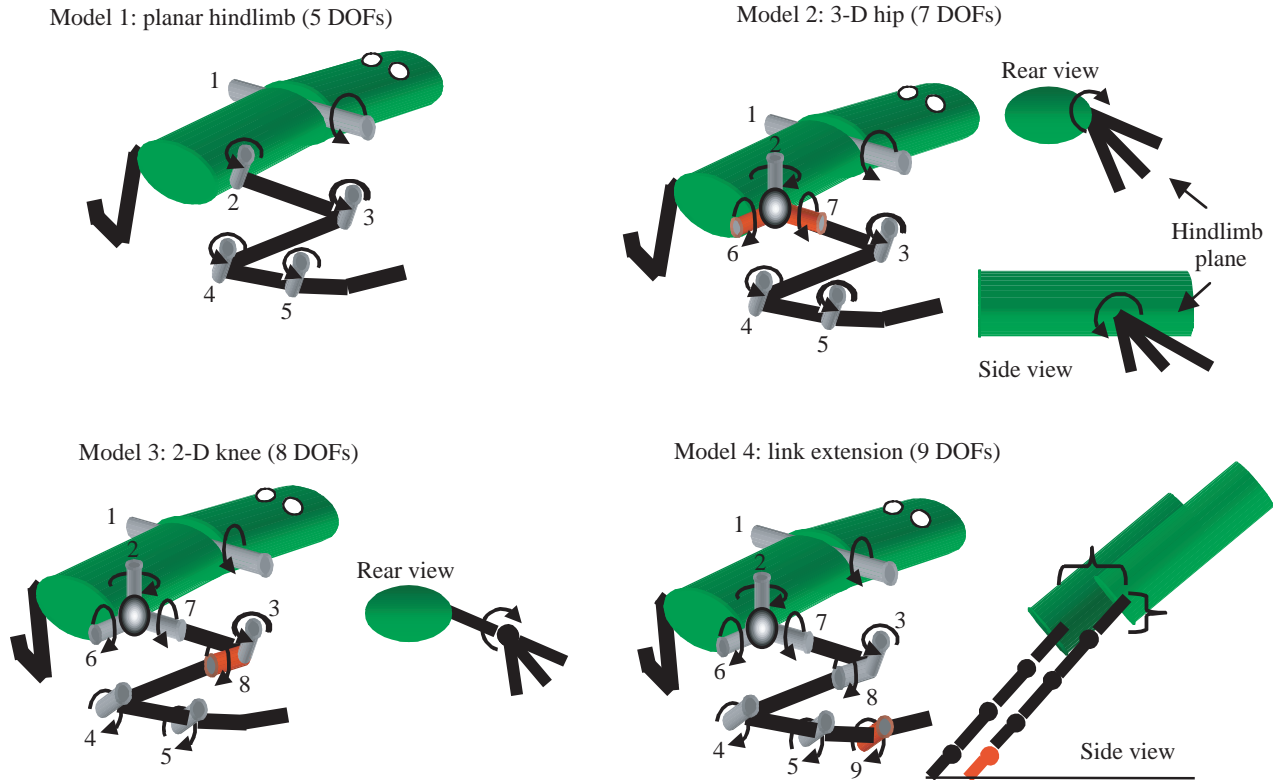Model 3: 2-D knee (8 DOFs)

Model 4: link extension (9 DOFs)

Fig. 5. The four frog models on which forward dynamic simulations of jumping were performed. Here, we assume that the hindlimbs are symmetrical with respect to jumping. Hence model 1 had five rotational degrees of freedom (DOFs). These DOFs are flexion–extension at the iliosacral (1), hip (2), knee (3), ankle (4) and tarsometatarsal (5) joints. Model 2 had seven rotational DOFs. The two extra DOFs compared with model 1 (6 and 7, shown in red) are abduction–adduction and external–internal rotation at the hip. These DOFs permitted the plane of the hindlimb to be rotated under the body and at different angles relative to the ground. Model 3 had eight rotational DOFs. The extra DOF compared with model 2 (8, shown in red) is external–internal rotation at the knee. This DOF permitted the distal limb, consisting of the tibiofibula, astragalus segment and foot, to be rotated further under the body. Model 4 had nine rotational DOFs. The extra DOF compared with model 3 (9, shown in red) is flexion–extension at the metatarsophalangeal joint. This DOF permitted the frog to move its center of mass longer distances during the ground-contact phase of the jump and to achieve higher take-off velocities

passively applied hip extension. This was in agreement with previously reported data (Lieber and Shoemaker, 1992). Thus, we modeled the virtual hip joint in the extension–flexion plane as a revolute joint in which the position of the instantaneous center of rotation was fixed. The location of the instantaneous center of rotation was positioned 1.5 mm along the long axis of the femur from its most proximal point.

The rotational DOFs of the femur about its x and y axes represented hip external–internal rotation and hip abduction–adduction, respectively. The sequence of instantaneous centers of rotation for both external–internal rotation and abduction–adduction (first column, bottom two panels of Fig. 3) tended to cluster into a single, circumscribed region (areas 1.1 ± 0.26 mm^2 and 1.9 ± 0.3 mm^2, respectively, means ± S.E.M., $N=8$ frogs). For abduction–adduction, the instantaneous centers clustered in a position located approximately 1.5–2 mm from the femur's most proximal point. For external–internal rotation, the instantaneous centers clustered at a position near the center of the acetabulum. The tight clustering indicated that the location of the instantaneous center of rotation about each joint axis was approximately constant throughout the passively

applied range of motion. Thus, the hip joint could be modeled as a gimbal joint, which consists of three independent revolute joints. The intersection of the instantaneous centers of rotation for each revolute joint was positioned 1.5 mm along the long axis of the femur, from its most proximal point, and at the level of the central acetabulum.

Behavior and modeling of the knee joint

For the majority of frogs examined (four out of six) the flexion–extension kinematics at the knee conformed most closely to a rolling joint. As shown in Fig. 3 (top row, second panel from left), the positions of the instantaneous centers of rotation for the knee traversed a curve that approximately traced the joint surface of the proximal bone. The instantaneous center of rotation was located at one end of this curve at the extreme range of flexion and 'rolled' to the other end of the curve, along the surface of the proximal bone, as the moving segment was extended. Thus, we modeled the flexion–extension of the virtual knee as a rolling joint so that the tibiofibula segments smoothly traversed an arc of 70 ° along the surfaces of the distal femur.

The rotational DOF of the tibiofibula about its x axis was termed knee external–internal rotation. The range of knee external–internal rotation was approximately $60°$ ($±30°$ from the reference configuration) before significant torsion of connective tissues surrounding the knee joint was noticed. The locations of the instantaneous centers of rotation tended to cluster into a single, circumscribed region located at the level of the mid-tibial crest (second column, bottom panel of Fig. 3). Thus, we modeled the knee joint as a type of universal or Hooke's joint, which consists of two independent joints. Knee flexion and extension occurred about a rolling joint, and knee external–internal rotation occurred about a revolute joint whose instantaneous center of rotation was located at the instantaneous center for knee flexion. That is, as the instantaneous center for knee flexion traversed the surface of the distal femur, the instantaneous center for external rotation was carried along with it. The measured range of knee adduction, i.e. rotation about the y axis, was $45–50°$ (see second column, middle panel in Fig. 3).

Behavior and modeling of the ankle, tarsometatarsal, metatarsophalangeal and iliosacral joints

For the majority of frogs examined (three out of five), the flexion–extension kinematics at the ankle conformed most closely to a rolling joint. As shown in Fig. 3 (top row, third panel from left), the positions of the instantaneous centers of rotation for the ankle traversed a curve that approximately traced the joint surface of the proximal bone. The location of the instantaneous center of rotation was located at one end of this curve at the extreme range of flexion and 'rolled' to the other end of the curve, along the surface of the proximal bone, as the moving segment was extended. Thus, we modeled the virtual ankle joints as a rolling joint so that astragalus segments smoothly traversed a $90°$ arc along the surfaces of the tibiofibula.

The tarsometatarsal joint was modeled as revolute joint. The instantaneous center of rotation was positioned at the point of contact between the distal end of the astragalus segment and the proximal metatarsals (see location of red dot in Fig. 3, top row, right panel).

Because of the difficulty in accurately measuring kinematics about this small and delicate metatarsophalangeal joint in the jig (the ends of the two bones were less than 1 mm in diameter), we simply modeled this joint as a revolute joint. The position of the instantaneous center of rotation was placed at the point of intersection between the bone segments.

The measurement of iliosacral kinematics is shown in Fig. 3 (bottom right panel). Flexion–extension of the vertebral segment occurred about its x axis. We examined iliosacral kinematics in four frogs. The instantaneous center of vertebral rotation did not follow a consistent path among these frogs. This variability might be due to the fact that the iliosacral joint is to some extent a true gliding joint. In a gliding joint, the x- and y-translations and rotations within the plane are independent of each other. To avoid the complexities associated with modeling such a joint, we

approximated the iliosacral joint as a revolute joint, in which the center of rotation was located at the contact point between the tip of the iliac crest and the transverse processes of the sacrum. The measured range of motion was $90°$ ($30°$ extended relative to the reference position and $60°$ flexed).

Four models of jumping frogs

A schematic diagram of the kinematic degrees of freedom making up the four skeletal models is shown in Fig. 5.

Model 1: planar hindlimb model

For simplicity in modeling, it has sometimes been assumed that the hindlimb joints of frogs extend within a single plane during jumping and that other DOFs at the hip and knee could be ignored (Alexander, 1995). In model 1, we assessed this possibility by constraining all the hindlimb joints to only flex and extend. The initial flexion angles at the start of the simulations were determined for the hip, knee, ankle, tarsometatarsal and iliosacral joints (see *Kinematic and inverse dynamic analyses of jumping frogs*). If the pelvis of model 1 was positioned at $15–20°$ to the ground, similar to the real frog, then the plane in which the hindlimb was oriented would also be at $20°$ to the ground. Extension of the hindlimb within this plane would necessarily lead to a low take-off angle and, hence, a short jump distance (blue trace in Fig. 6D). Take-off angles of $42°$ are necessary for maximal-distance jumping. Thus, to test whether model 1 could in theory permit maximal-distance jumping, it was necessary to invoke an unphysiological starting position in which the pelvis was tilted at $42°$ to the ground and the hindlimbs rested in an unnatural starting position (see Fig. 6A).

We first examined the range of dynamic behaviors that model 1 could produce from its starting position. A batch of 1000 simulations was run in which we randomly varied the magnitude of the extensor torque steps applied about the iliosacral, hip, knee and ankle joints. Trajectories of the virtual frog's COM are shown in Fig. 6B. For illustrative clarity, only 100 trajectories are shown starting from the onset of the torque steps for a period of 95 ms. This is the approximate duration from onset of electromyographic activity to toe-off in the real frog. The COM followed a similar initial path for each simulation run. This was because model 1 permitted hindlimb movements in only a single plane (i.e. extension). Variations in the magnitude of the extensor torques between simulation runs produced variations in the magnitude of the GRF but not in the GRF orientation. Consequently, the vertical and horizontal velocities of the COM were linearly correlated among the simulation runs (Fig. 6E, $r^2=0.97$, $P<0.001$; i.e. initial take-off angles were the same for each run and equal to the angle of pelvis tilt).

We tested whether model 1 could reproduce maximal-distance jumping. To do this, we used the torque values generated by the real frog to drive the forward dynamics of model 1. Only the hindlimb 'extensor' torques and the iliosacral torque were used to drive the model dynamics (i.e.

Fig. 6. Jumping performance of model 1. (A) Model 1 did not permit rotations other than flexion–extension at the hindlimb joints. In a normal starting position (shown in Fig. 7A), jump distance was very short compared with the real frog (blue *versus* black recordings in D). Hence, to assess better its jumping potential, model 1 was placed in an unnatural starting position in which the plane of the hindlimbs and the long axis of the pelvis were oriented at 42° to the ground. The purple, orange and green arrows represent the ground reaction forces (GRFs) at the starting position that were produced by a unit extensor torque (1 N m) about the hip, knee and ankle joints, respectively. GRFs are in normalized units (i.e. N per N m of torque), so a torque value of 0.009 N m at the hip will produce 0.15 N of GRF (i.e. $0.009\,\mathrm{N\,m}\times15\,\mathrm{N\,N^{-1}\,m^{-1}}$). At the starting position, a unit hip extensor torque produced the largest propulsive GRF. (B) The path of the center of mass (COM) of the frog during the ground-contact phase of the jump for 100 simulation runs in which the magnitudes of the extensor torques driving each relaxed DOF were randomly varied. The red path in B–D represents the simulation run in which the actual torques produced by the real frog were used to drive the model. The blue path represents a simulation run in which model 1 was placed at a more natural starting position in which the pelvis was oriented at 15° to the ground. (C) The vertical V_V and horizontal V_H velocity of the COM for the red and blue runs did not match the velocity of the real frog (black lines). (D) The predicted jump distances for the red and blue runs were shorter than those for the real frog. (E) The vertical and horizontal velocities were tightly correlated (r^2=0.97, P<0.001) during simulations, signifying that take-off angles were the same for each run and equal to the angle of pelvis tilt. This occurs because the vectors of GRFs for a given torque are in the same direction for each joint (see A). (F) Accordingly, the magnitudes of vertical and horizontal velocities were tightly correlated to GRF (r^2=0.90, P<0.01 for vertical and r^2=0.81, P<0.01 for horizontal velocities).
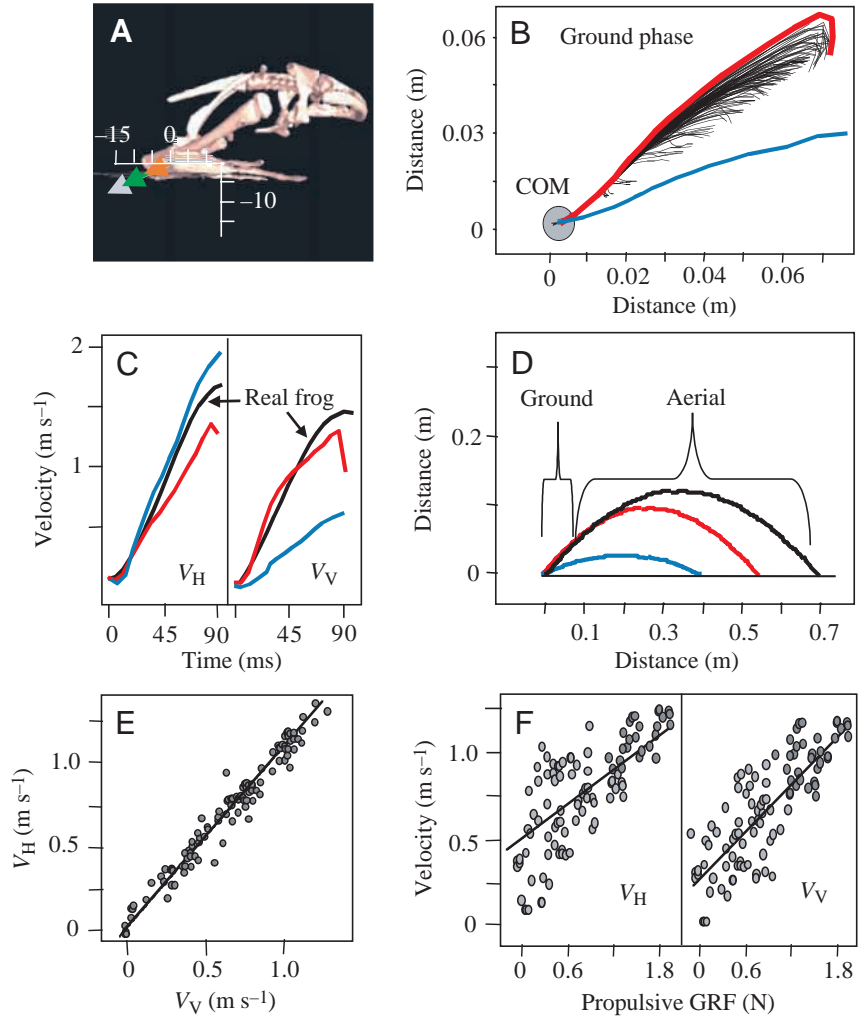

the other hindlimb DOFs were fixed, and torques about these DOFs were therefore zero). When model 1 was placed in a physiological starting position in which the pelvis was oriented at 15° to the ground, the take-off angle was also 15° and the jump distance was only 0.380 m (blue lines in Fig. 6B–D). Even when unphysiological starting positions were used (pelvis tilted at 42° to the ground; red lines in Fig. 6B–D), the jump distance was only 70% of that obtained by the real frog. The black lines in Fig. 6C,D represent the trajectory of a real frog jumping at 25°C. The peak total velocity (i.e. the vector sum of the vertical V_V and horizontal V_H velocities) of the 42° run was 1.83 m s⁻¹ compared with 2.33 m s⁻¹ for the real frog, and the trajectory of the COM during the ground-contact phase resulted in a predicted jump distance of 0.552 m compared with 0.704 m for the real frog. The inability to produce both maximal-distance jumping and a range of take-off angles suggests that additional DOFs and joints are critical for jumping.

Model 2: three-DOF hip joint

In the actual frog, the hip joint is not constrained to only extend during jumping; other DOFs at the hip might be critical for jumping performance. Model 2 captures the three-dimensional properties of the hip by adding the external–internal rotation and abduction–adduction DOFs. The remaining hindlimb joints were constrained to only flex and extend. The hip was positioned in its initial configuration as determined from the kinematic analysis: flexed by 32°, adducted by 18° and internally rotated by 15°. The knee and ankle were initially flexed by 155° and 150°, respectively.

We first examined the range of dynamic behaviors that model 2 could produce. To do this, a batch of simulations was run in which we randomly varied the magnitude of the torque steps applied about each rotational DOF. Trajectories of the virtual frog's COM are shown in Fig. 7B. Both internal and external rotation torques were applied about the femur's x axis, and both abduction and adduction torques were applied about

Fig. 7. Jumping performance of model 2. (A) Model 2 was placed in a normal starting position. The colored arrows represent ground reaction forces (GRFs) as in Fig. 6. In addition, the GRF per unit N m of torque is shown for hip external rotation (yellow) and hip adduction (blue). (B) The path of the center of mass (COM) of the frog during the ground-contact phase for 500 simulation runs in which the magnitudes of hindlimb torques were randomly varied. A large range of take-off angles was produced from a single starting position. The blue path in B–D represents the simulation run in which the actual torques produced by the real frog were used to drive the relaxed degrees of freedom. The red path represents a simulation run in which hip external rotation was increased fourfold compared with that produced by the real frog during a jump. (C) The vertical V_V and horizontal V_H velocities of the COM for the red simulation run matched those of the real frog (black lines) better than the blue run. However, this required an unphysiological level of external rotation torque. (D) The predicted jump distances for the red and blue runs were smaller than those for the real frog. (E) Unlike model 1, the vertical and horizontal velocities for each simulation run were not correlated with one another (i.e. take-off angle varied from trial to trial). This was because individual torque components produced different ratios of vertical to horizontal GRF (see arrows in A). (F) The magnitudes of the hip (HE) and ankle extensor (AE) torques were significantly ($P<0.01$; $r^2=0.69$ and $r^2=0.63$, respectively) correlated with variations in the peak horizontal velocity among the simulation runs. Only the magnitude of the hip external rotation (HR) torque was significantly ($P<0.01$, $r^2=0.59$) correlated with variations in the peak vertical velocity.
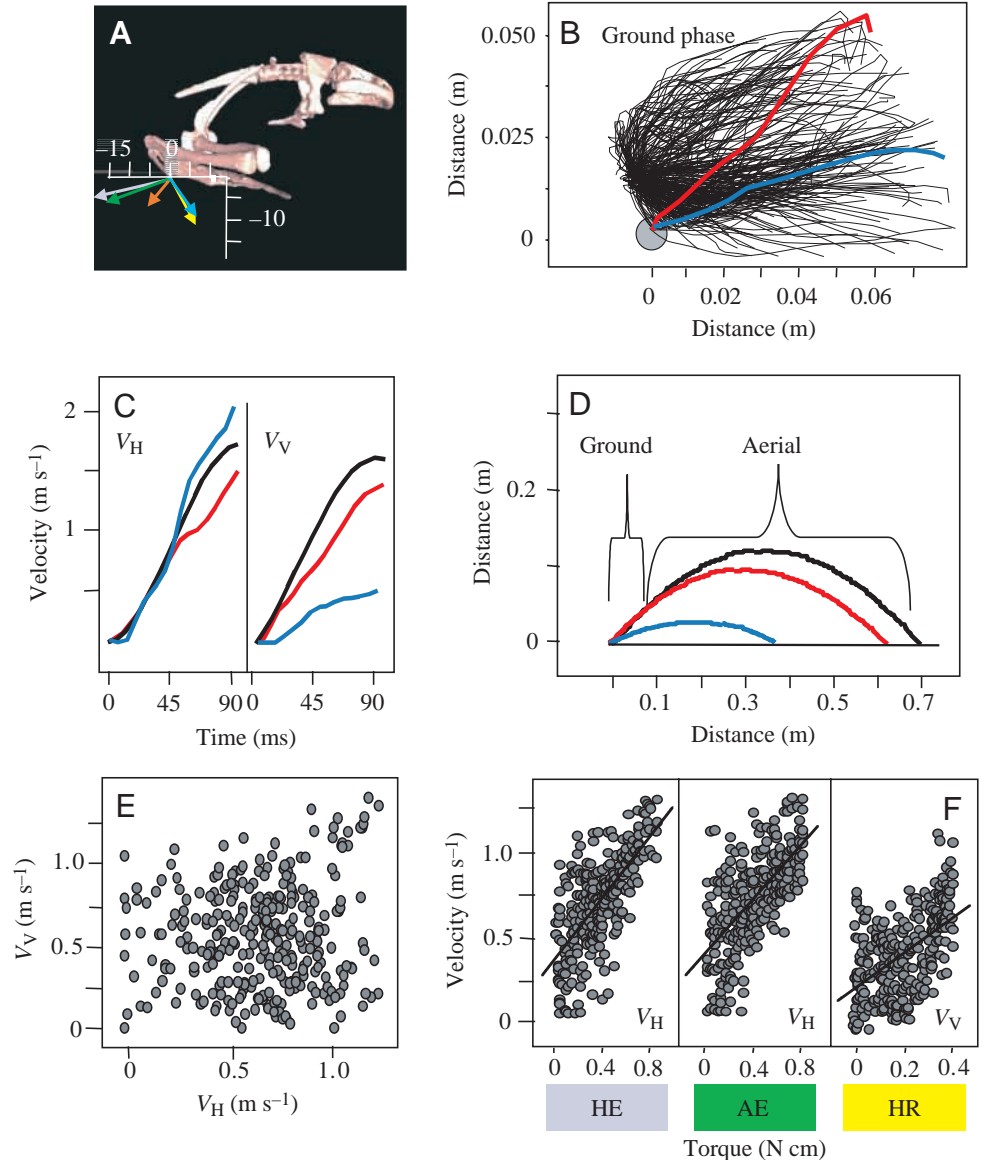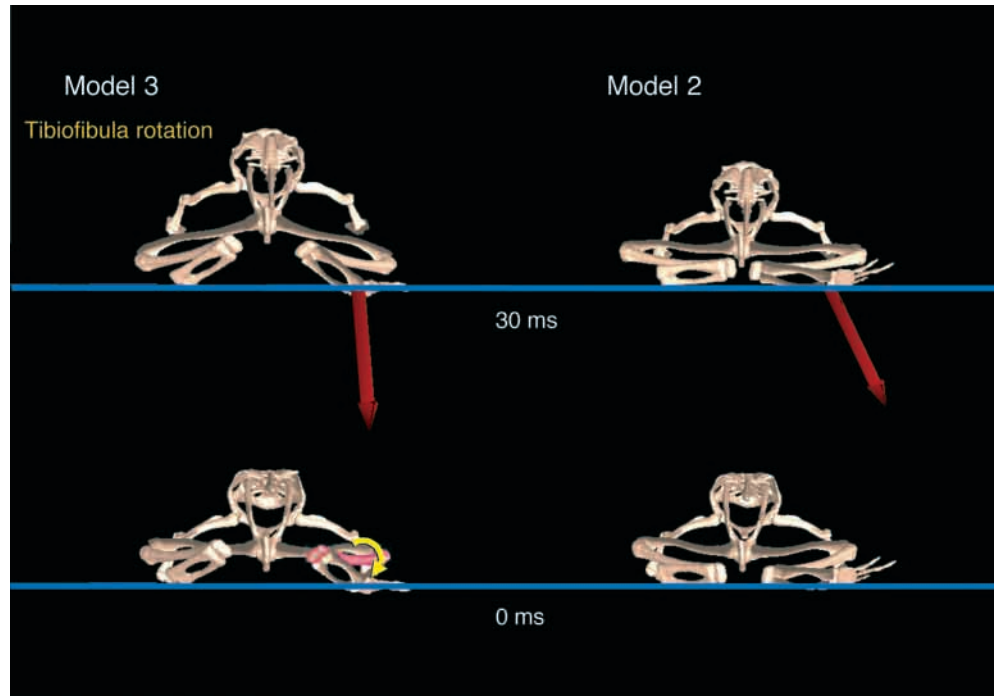
the femur's *y* axis. Five hundred trajectories are shown starting from the onset of the torque steps for a period of 95 ms. What is most evident from Fig. 7B is that a large range of take-off angles was produced in this model compared with model 1. The take-off angles ranged from 0 to 90° relative to the ground. The peak vertical and horizontal velocities of the COM showed no significant correlation among simulation runs (see Fig. 7E) because, unlike model 1, the individual hindlimb torques produced different ratios of horizontal to vertical GRF.

We examined the GRFs produced by each hindlimb torque at the starting limb configuration. Fig. 7A shows the GRF vectors produced by a unit hip extensor (purple), knee extensor (orange), ankle extensor (green), hip external rotation (yellow) and hip adduction (blue) torque. The GRF vectors are based

on unit torque inputs, but it is important to keep in mind that these vectors will be scaled by the actual torque values shown in Fig. 1 (e.g. the GRF due to a unit hip extensor torque is $16.93\,N\,N^{-1}\,m^{-1}$ and thus the GRF due to 0.009 N m of hip extensor torque is 0.15 N). A unit hip extensor torque produced a large horizontal and smaller vertical force (ratio 15.5:6.8). A unit ankle extensor torque produced a similar ratio of horizontal to vertical force (13.2:8.0). A unit knee extensor torque produced a relatively small horizontal force (2.1 N) and a vertical force (7.2 N) comparable with that produced by hip and ankle extensor torques. The knee extensor torque produced a very large lateral force (18.2 N) compared with the lateral forces produced by the hip (–5.1 N; negative values represent medially directed forces) and ankle extensor unit torques

Fig. 8. Internal rotation of the tibiofibula at the starting jump position enhances the vertical component of the ground reaction force (GRF). Left column, model 3; right column, model 2; bottom panels, position of models at the start (0 ms) of the jumping simulation; top panels, position of models and orientation of the GRF (red arrow) 30 ms into the simulation. Model 3 had an extra degree of freedom about the knee compared with model 2, wherein the tibiofibula (the bone colored pink on the right side of model 3) was internally rotated about its long axis. By bringing the foot under the frog's body, this internal rotation increased the vertical component of the GRF relative to the horizontal component during the early portion of the jumping simulation. The GRF shown for both models was calculated in response to the same extensor torque pattern applied about the hip, knee and ankle joints.

(5.9 N). Both hip external rotation and hip adduction unit torques produced relatively large vertical forces (11.1 and 9.3 N, respectively), but horizontal forces that opposed forward translation (–8.0 and –9.1N, respectively).

On the basis of the static descriptions of torque transmission, we predicted that hip and ankle extensor torques should accelerate the COM most strongly in the horizontal direction and that hip external rotation and adduction torques should accelerate the COM most strongly in the vertical direction. This relationship was in fact observed (see Fig. 7F). The magnitude of both the hip and ankle extensor torques was significantly ($P<0.01$) correlated with the peak horizontal velocity of the COM ($r^2=0.69$ and $r^2=0.63$, respectively). The magnitude of the hip external rotation torque was significantly correlated with the peak vertical velocity ($P<0.01$, $r^2=0.59$). The hip adduction torque did not show a significant correlation with peak vertical velocity. Thus, increasing the external rotation torque will produce higher take-off angles and lower acceleration take-offs, and increasing ankle and hip extensor torques will produce lower take-off angles and higher acceleration take-offs. However, it is important to keep in mind that the majority of the jumping muscles are biarticular, and independent regulation of hindlimb torques may not be possible in the real frog.

We tested whether model 2 produced maximal-distance jumping when the real jumping torques (shown in Fig. 1) were used to drive its forward dynamics. To our surprise, we found that model 2 did not produce maximal-distance jumping. Instead, the take-off angle was approximately $13°$ and the vertical velocity was only $0.4\,\mathrm{m\,s^{-1}}$ (blue trajectories in

Fig. 7B–D). This resulted in a predicted jump distance of 0.370 m (Fig. 7D). If we increased the hip external rotation torque by four times that observed in the real frog, model 2 produced jumps that more closely resembled maximal-distance jumps (red trajectory in Fig. 7B–D). That we could not produce maximal-distance jumping in model 2 using physiological estimates of hindlimb torque values suggested that additional DOFs must be added to the frog model.

Model 3: two-DOF knee joint

The frog knee joint exhibits an overflexion mechanism in which the calf is rotated along its long axis and carried over the dorsal aspect of the thigh in the extreme ranges of knee flexion (Lombard and Abbot, 1906). This over-flexion mechanism may enhance the jumping performance of the model. Thus, we added this DOF at the knee joint in model 3. The knee was then internally rotated by $30°$, the estimated rotation angle at the starting position of the jump (see Materials and methods). As shown in Fig. 8, this rotation brought the foot more underneath the body and more within the sagittal plane compared with model 2 and, thereby, increased the vertical component of the GRF. As described above, there is an additional DOF in the knee in the adduction–abduction plane. Preliminary simulations showed that this DOF had little effect on jumping performance and thus, for computational simplicity, we fixed this DOF so that the adduction angle was constant at $90°C$. The remaining joint angles were the same as the initial angles in model 2.

We first examined the range of dynamic behaviors that model 3 could produce by randomly varying the magnitude

Fig. 9. Jumping performance of models 3 and 4. (A) Models 3 and 4 were both placed in the normal starting position. The colored arrows represent the ground reaction forces (GRFs) as in Figs 6 and 7 for both models. Note that the GRF generated by internal rotation at the knee is mostly lateral in direction (i.e. out of the page) and hence is not shown. (B) The path of the center of mass (COM) of model 3 during the ground-contact phase for 500 simulation runs in which the magnitudes of hindlimb torques were randomly varied. The red path in B–D represents the simulation run in which the actual torques produced by the real frog were used to drive the degrees of freedom (DOFs) in model 3. The blue path represents the simulation run in which the same torque pattern was used to drive model 4. (C) The vertical V_V and horizontal V_H velocities of the COM for the red simulation run matched those of the real frog (black lines) over the first 70 ms. At this time, model 3 was maximally extended and the simulation ended. The vertical and horizontal velocities of the COM of model 4 more closely matched those of the real frog over the entire 90 ms take-off phase (i.e. addition of the distal joint allowed model 4 to extend

further during the remaining 15 ms of the jump). (D) The predicted jump distance for model 3 was less than that of the real frog. However, the predicted jump distance for model 4 closely approximated that of the real frog. (E) As in model 2, vertical and horizontal velocities in model 3 were not correlated. (F) The magnitude of only the hip extensor (HE) torque was significantly ($P<0.01$, $r^2=0.71$) correlated with variations in the peak horizontal velocity among the simulation runs in model 3. No single torque component was significantly correlated with variations in vertical velocity. In trials in which the ankle extensor (AE) torque was greater than 0.3 N cm (boxed region in the V_V *versus* AE torque graph), the time (T) taken for the ankle to extend past 90 ° was significantly ($r^2=0.61$, $P<0.05$) correlated with variations in vertical velocity (right panel). The later the ankle extended during the ground-contact phase, the larger the vertical velocity.
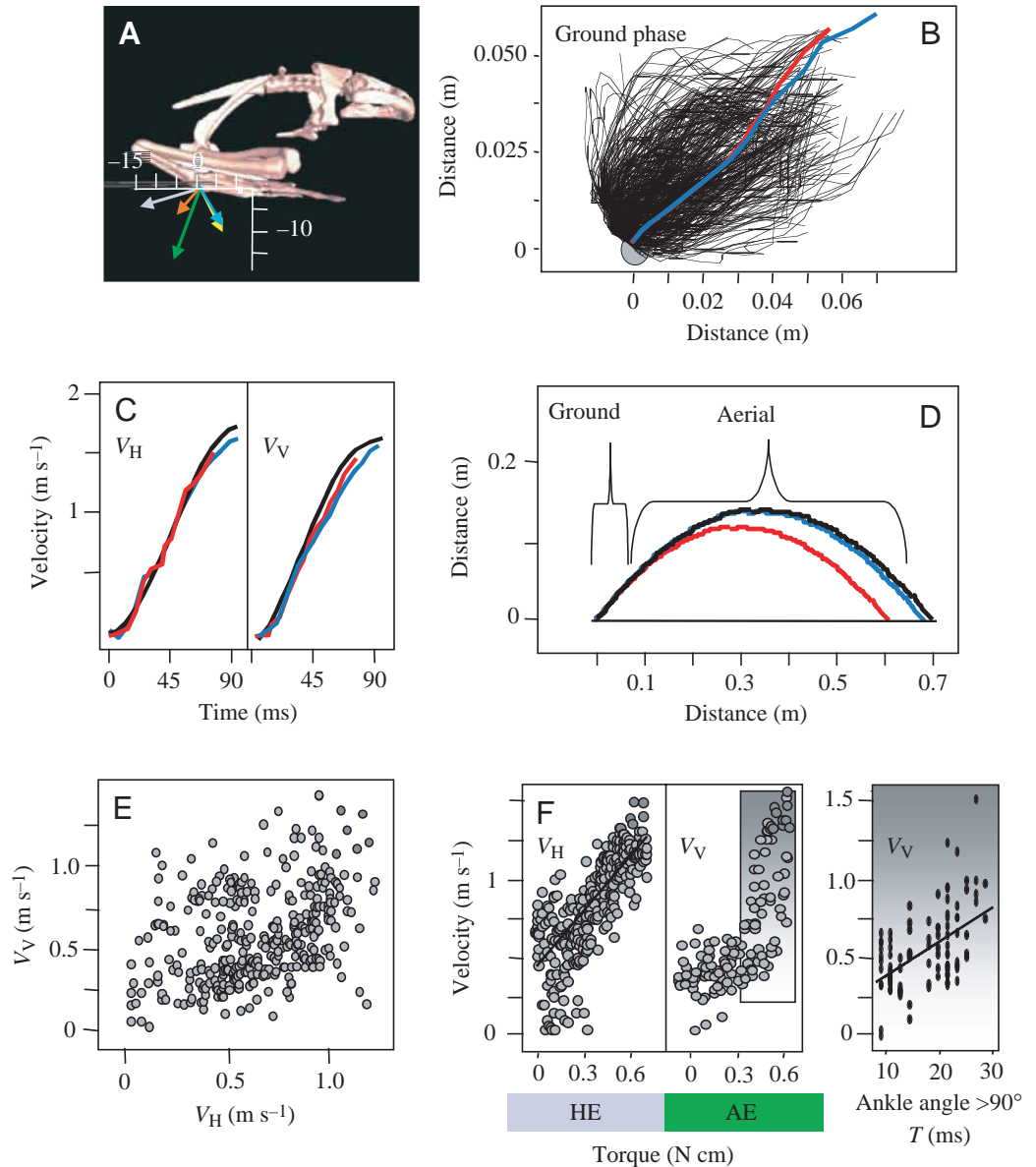
of torque steps applied about each rotational DOF. The trajectories of the virtual frog's COM, which were generated by driving the forward dynamics of the model with randomized torque steps, are shown in Fig. 9B. Both internal and external rotation torques and both abduction and adduction torques were applied at the hip. Five hundred trajectories are shown starting from the onset of the torque steps for a period of 95 ms. Similar to model 2, we found that model 3 produced a large range of take-off angles (0–90 °) from a single starting position. However, unlike model 2, we found that model 3 produced

near-maximal-distance jumping using physiological estimates of hindlimb torque values.

When the hindlimb torques computed in the real frog were used to drive the forward dynamics of model 3, the simulated jump closely matched that of the real frog. Fig. 9C shows the horizontal and vertical velocity of the COM of model 3 (red lines) compared with the real frog (black lines). Fig. 10 shows the hindlimb joint angles of model 3 (red lines) compared with the real frog (black lines). The trajectory of the COM and the hindlimb joint angles were very similar for the first 70 ms of the
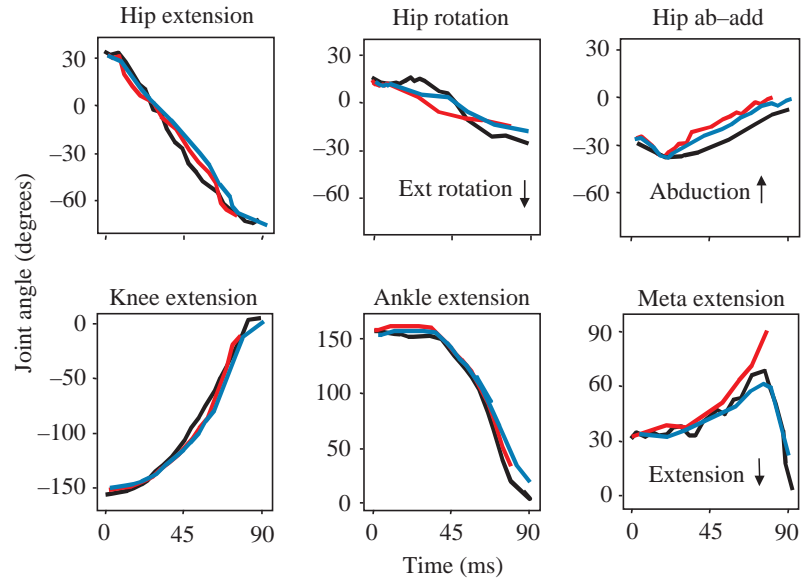
Fig. 10. Comparison of the joint kinematics of model 3 (red lines), model 4 (blue lines) and experimental frogs (black line represents data from one frog). The forward dynamics of models 3 and 4 were driven with the joint torque pattern estimated from the kinematics of experimental frogs. The hindlimb joint angles of both models closely corresponded to the experimental data for the first 70 ms of each simulation run. After 60–70 ms, the metatarsal joint (Meta) of experimental frogs begins to extend (lower right panel). Model 3 did not capture this reversal of tarsometatarsal joint motion because the metatarsal–phalangeal segment was fixed to the ground. Model 4, which allowed passive rotation of the metatarsal segment above the ground (i.e. no active torques were applied about the tarsometatarsal joint), did capture this kinematic effect. ab–add, abduction–adduction; Ext, external.

jump. After that time, the hindlimb of model 3 was maximally extended and the simulation was terminated. This early termination was due to the fact that the metatarsophalangeal segment of model 3 was rigidly secured to the ground. Thus, unlike the real frog, the tarsometatarsal joint of model 3 did not extend during the last 10–15 ms of the jump (this joint flexes during the first 60–70 ms of the jump; see Fig. 10). The jump of model 3 had a predicted distance of 0.612 m compared with 0.704 m in the real frog (Fig. 9D). Before examining how adding the metatarsophalangeal joint enhances jumping performance, we first examined in more detail why model 3 produced a much better jump than model 2.

We examined how the GRFs produced by the individual hindlimb torques were different in model 3 compared with model 2. The GRF vectors produced by unit torque inputs are shown in Fig. 9A (purple, hip extensor; green, ankle extensor; orange, knee extensor; yellow, hip external rotation; blue, hip adduction). The GRFs produced by hip extensor, knee extensor, hip external rotation and hip adduction torques were similar to the GRFs produced by the same torques in model 2, i.e. the ratio of vertical to horizontal to lateral force for each torque was similar in both models. However, an ankle extensor torque in model 2 produced GRFs that were dramatically different from those produced in model 3. A unit ankle extensor torque produced a vertical force that was twice that produced in model 2 (15.8 N compared with 8.0 N). Thus, internal rotation of the tibiofibula (Fig. 8, left panel) allowed the ankle torque to produce a GRF with a larger vertical than horizontal component (15.8:5.0). In terms of absolute values, the real torque pattern in the frog produced a total GRF at the starting limb position in which the vertical component was 0.99 N for one hindlimb (1.98 N for both limbs) and the horizontal component was 1.01 N (2.02 N for both limbs). The same torque pattern produced a GRF in model 2 that had a vertical component of only 0.78 N and a horizontal component of 1.23 N. Thus, the extra DOF at the knee permitted the ankle

torque to contribute more to the vertical acceleration of the center of mass, which in turn produced a more optimal take-off angle (42 °) for maximal-distance jumping.

On the basis of the static descriptions of torque transmission in model 3, we predicted that variations in the magnitude of the hip extensor torque should be related to variations in the peak horizontal velocity of the jump. This relationship was observed (see Fig. 9F, left panel; significant at $P<0.01$, $r^2=0.71$). We hypothesized that variations in the ankle extensor torque, because of its increased contribution to the vertical GRF at the starting position, should be related to variations in the peak vertical velocity of the jump. However, we found this was not the case (see Fig. 9F, middle panel). Instead, a combination of kinematic and dynamic factors was related to variations in the vertical velocity. In simulation runs in which the ankle extensor torque was greater than 0.3 N cm, the most notable factor correlated with variations in V_V was the time for the ankle angle to extend past 90 ° from a starting angle of 150 ° (see Fig. 9F, right panel). This was because the magnitude of the vertical force produced by the ankle torque depended critically on the ankle angle. As the ankle extended during the jump, the ankle torque produced less vertical and more horizontal force. Thus, if the ankle extended early or at an initially high rate in the jump, then the ankle torque accelerated the COM more in the horizontal direction. If the ankle extended later or at a slower initial rate, then the ankle torque accelerated the frog more in the vertical direction. The initial rate of ankle extension depended on the magnitude of the hip and knee extensor torques. When these other torques were high, the ankle extended later and higher take-off angles were produced. If these torques were low and the ankle torque was the same value, the ankle extended earlier and lower take-off angles were produced.

Model 4: addition of the metatarsophalangeal joint

Freeing the metatarsal segment so that it can lift off the

ground should, at the least, function passively to increase jump distance. Jump distance is the sum of the horizontal distances covered by the COM during the ground-contact and aerial phases. Freeing the metatarsal segment should increase the horizontal distance covered by the COM during the ground-contact phase. If the vertical distance covered by the COM is also increased, the duration of the aerial phase and therefore the distance covered during the aerial phase will be increased as well. Freeing the metatarsal segment should also allow the other joint torques to produce GRFs for longer. We examined how releasing the metatarsal segment and adding a metatarsophalangeal joint in model 4 enhanced jumping performance. The torque values calculated for the iliosacral, hip, knee and ankle joints in the real frog were used to drive the forward dynamics. No torques were applied about the tarsometatarsal joint, and it therefore contributed only passively to jumping performance. The simulation resulted in a predicted increase in jump distance of 0.101 m compared with jumps with the metatarsal segment fixed to the ground (see Fig. 9D; trajectory with metatarsal fixed to the ground, red line; metatarsal freed, blue line). The increase in jump distance was due to an increase in take-off velocity, an increased horizontal distance covered during the ground-contact phase and an increased height at take-off, which prolonged the aerial phase.

Discussion

In this study, we used a modeling approach to test what the appropriate hindlimb model was for producing maximal-distance jumping and for producing a flexible range of take-off angles. We found that, to produce maximal-distance jumping, the skeletal system of the frog must minimally include a gimbal joint at the hip (three rotational DOFs), a universal Hooke's joint at the knee (two rotational DOFs) and pin joints at the ankle, tarsometatarsal, metatarsophalangeal and iliosacral joints. In addition, we found that a unique mechanism at the knee joint provided an opportunity to flexibly control the take-off angle that was not possible without this mechanism. In the following, we discuss the approach used in this study and the implications of our results for maximal-distance jumping and locomotor control in the frog.

Reverse engineering approach to functional morphology

Reverse engineering is the process of disassembling a product to determine how it is designed from the component level upwards. In this study, we disassembled the skeletal system of the frog into individual rotational DOFs at the joints and then used these DOFs to construct progressively higher-dimensional models. We tested the range of behaviors, both dynamic and static, that each model structure could produce and whether the model permitted maximal-distance jumping, which is a behavior of great interest to integrative muscle physiologists (see below). We found this modular approach to be particularly useful because frog jumping is kinematically quite different from human jumping. In particular, we found

that the internal rotation DOF at the frog knee joint, which is insignificant in humans, played a very important role during frog jumping. Adding this DOF to the frog knee joint permitted the generation of a wide range of take-off angles not attainable in simpler models and permitted a take-off angle of 42 %, which is necessary for maximal-distance jumping, when using physiological estimates of torque values to drive frog motion.

The approach in which modules are added to an existing structure cannot be used to attribute a single function to any individual module. Each module has its particular significance for, and influence on, the functional totality, but at the same time each module is regulated and limited in its function by the other modules (Savazzi, 1999). For example, adding the extra DOF at the knee permitted the expression of maximal-distance jumping by allowing the limb to enter a particular starting configuration otherwise not attainable (Fig. 8, left panel). In this configuration, the extensor torque about another DOF (the ankle) resulted in a larger vertical GRF compared with models without the extra DOF at the knee and consequently higher take-off angles close to 42 %. At the same time, we found that transmission of the ankle torque to the GRF was configuration-dependent. Thus, if extensor torques about other DOFs (hip and knee) were too small, the ankle extended early in the jump and the ankle torque produced a more horizontal GRF and, consequently, lower take-off angles. Therefore, both a correct balance of hindlimb torques and a correct starting configuration were necessary for the expression of maximal-distance jumping.

In addition, considerable care must be used when interpreting our simulation results to differentiate between kinematic effects and the effects of the reduced power associated with removing DOFs. Removing a given DOF eliminates motion about this DOF (kinematic effect) but also eliminates joint work and power produced about this DOF. We found that the distance of simulated jumps declined as DOFs were removed from the model. One interpretation is that motion about these DOFs (either pre-jump to position the joints into the starting configuration or during the jump) are necessary for the kinematic expression of jumping. However, an alternative explanation is that removing DOFs also removes the work generated around these DOFs and thus removes mechanical energy from the system. Hence, in theory, this reduced work, rather than kinematic constraints, could be responsible for the reduced jump distance.

We assessed this possibility and found it not to be the case for the secondary DOFs at the knee and hip. For instance, model 3 was able to jump a far greater distance and generate far greater power than model 1. The increase in power was not due to added power generated about the secondary DOFs (two at the hip and one at the knee). In model 3, the joint power directly generated by the internal rotation of the knee was only 5 % of the total joint power, and the combined joint power generated by hip rotation and abduction–adduction torques appears to be negative. Hence, it is not the power generated around the added DOFs that improved performance, rather it

is the relief of kinematic constraints that enables the extensor DOFs to increase their power output.

Maximal-distance jumping

Comparative physiologists have long been interested in frog jumping because the frog is thought to have become well adapted for explosive jumps. Muscle, connective tissue, skeletal and neural are possible modifications to the system. Muscle properties that contribute to jumping have been addressed in other studies (Lutz and Rome, 1994, 1996a,b; Lutz et al., 1998). Potential skeletal adaptations for jumping may occur either in the morphology and mechanical characteristics of bone or in the DOFs and ranges of motion of the joints (Alexander, 1993). The present study did not address how the morphology and mechanical characteristics of bone contribute to performance (e.g. bone stiffness may govern whether and how bones store and release mechanical energy during movement) (see Blob and Biewener, 2001; Calow and Alexander, 1973). However, we did address three properties of the frog skeleton that enhanced jumping performance: (i) addition of a functional hindlimb joint to the limb complex, (ii) increased out-of-plane ranges of motion at the hindlimb joints and (iii) specialization of the iliosacral joint for jumping.

The astragalus and calcaneus are tarsal bones distal to the tibiofibula that have become elongated in the frog. In most other limbed vertebrates, the tarsal bones are relatively short and, with the metatarsal bones, form an essentially rigid foot segment. The skeletal changes in the frog yield a four-jointed rather than three-jointed hindlimb structure with five rather than four rigid segments (Gans and Parsons, 1966). Here, we showed that, by adding a functional tarsometatarsal joint to the hindlimb structure, jump distance could be increased 1.15-fold (by 0.1 m or 2 body lengths). One part of this increase was because the distance from the COM to the tip of the hindlimb was increased at the time of take-off, thereby increasing the take-off height and horizontal distance covered during the ground-contact phase. A second part of this increase was because the other hindlimb torques had a longer duration in which to produce GRFs and propel the frog (Howell, 1944; Alexander, 1995). Finally, a passive torque that is produced by a modest spring about this added distal joint could further increase jump distance by up to 0.08 m or 1.6 body lengths.

Out-of-plane rotations, other than flexion and extension, have been hypothesized to allow the hindlimb to move from a lateral, splayed position to a more anterior–posterior position in the frog (Gans and Parsons, 1966). Rotation of the limbs under the body will reduce the lateral GRFs produced by extensor torques and increase the vertical GRFs. In this study, the Jacobian matrix, which describes the differential properties of the limb linkage (Tsai, 1999), was calculated at the starting limb position for each model. The Jacobian matrix determines how joint torques are transmitted to the ground–limb interface and its form depends on the DOFs and configuration of the linkage. We found that, if out-of-plane motions were permitted at the hip and knee at the starting limb position (to match those

measured in experimental frogs), the same ankle torque produced one-third of the lateral force and three times the vertical force of that produced if out-of-plane motions were not permitted. Similarly, the same knee torque produced three-quarters of the lateral force and 1.25 times the vertical force. Thus, out-of-plane rotations provided a setting for producing a more balanced ratio of vertical to horizontal GRFs. To increase further the vertical forces so that higher take-off angles could be produced, a considerable amount of out-of-plane joint torque had to be produced (both hip adduction and external rotation torques). Both torque components produce large vertical forces at the starting limb position.

The iliosacral joint has been hypothesized to be important for frog jumping (Gans and Parsons, 1966; Emerson and de Jongh, 1980). The primary motion at this joint during jumping is, when viewed from the left side of the frog (nose pointing to the left), clockwise rotation of the trunk relative to the pelvis. This motion aligns the trunk with the GRF. If the trunk is not aligned, a moment is produced about the trunk that causes it to rotate away from the neutral position, which will in turn affect the efficacy with which the COM is accelerated (Emerson and de Jongh, 1980). The iliosacral joint might function in other ways as well. For example, trunk rotation moves the COM of the frog more directly over the ankle joint and therefore acts to oppose early ankle extension. If the ankle unfolds later or at a slower initial rate, the ankle torque produces relatively more vertical compared with horizontal force. Under these conditions, the frog can generate higher take-off angles. A sensitivity analysis supported this role (see below) and showed that larger iliosacral torques were associated with higher take-off angles.

Locomotor control

Rana pipiens use jumping as a general mode of terrestrial locomotion and not only for explosive escape responses. Even in the case of an escape response, the goal of frogs might not necessarily be to maximize jump distance but instead to maximize the horizontal acceleration (Emerson, 1978) or to concatenate several high-velocity, low-trajectory jumps (Gans and Parsons, 1966). Thus, selection of an appropriate skeletal model not only rests on whether this model can express maximal-distance jumping but also on whether it permits a wide range of jumping trajectories. In the process of testing this, we obtained insight into how the skeleton of the frog provides control opportunities to the neuromuscular system.

One of the main findings of this study was that the knee joint in the frog provided an opportunity for trajectory control that was otherwise not possible. The peculiarity of the frog's knee joint has long been recognized (Lombard and Abbot, 1906). In particular, the knee exhibits an over-flexion mechanism whereby the calf is carried dorsally over the thigh in the extreme ranges of knee flexion. This mechanism is thought to be important for wiping movements to the cloaca and back (Fukson et al., 1980; Giszter et al., 1989). However, even in the resting position of the frog, the tibiofibula was internally rotated by approximately 25–30 °. This degree of rotation was

Fig. 11. The sensitivity of jumping performance to variations in the magnitudes of the iliosacral extensor torque and the hindlimb torques examined using model 4. The torque pattern in Fig. 9 was used to drive the forward dynamics, and individual torques were scaled in amplitude by a factor of 0.80–1.20. HR, hip external rotation torque; HA, hip adduction torque; HE, hip extensor torque; KE, knee extensor torque; AE, ankle extensor torque; IE, iliosacral extensor torque. The take-off angle (trajectory of the center of mass, COM) was most sensitive to variations in the amplitude of the hip external rotation torque (i.e. the range of take-off angles was largest when HR was scaled from 0.80 to 1.20 of its base value). The horizontal velocity V_H was most sensitive to variations in the hip extensor torque. The vertical velocity V_V was most sensitive to variations in the hip external rotation torque and the knee extensor torque.
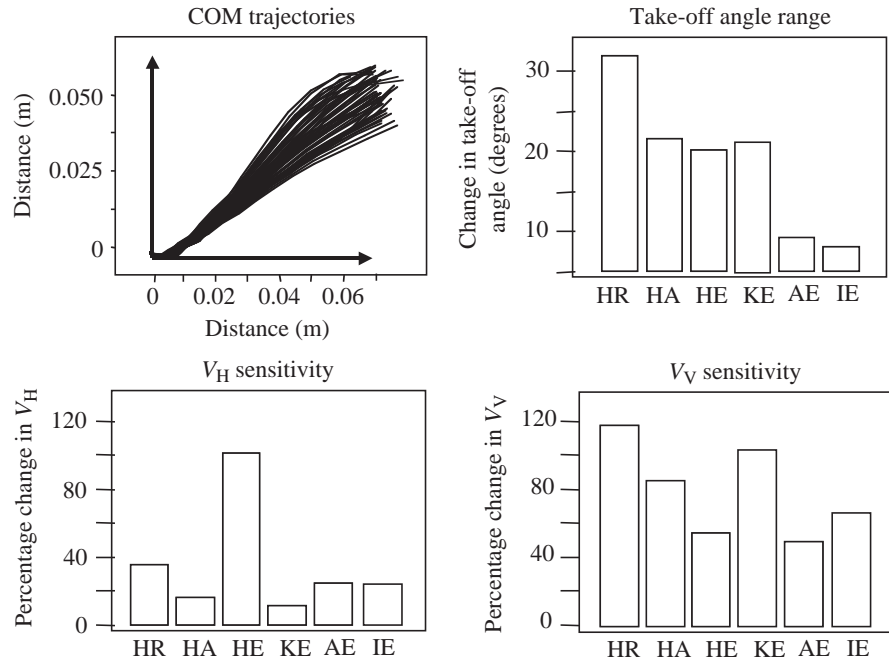
sufficient to double the vertical force contributed by the ankle extensor torque at the starting limb position. Without this force, the remaining torque components could not generate enough vertical force to accelerate the frog vertically, and only trajectories between 0 and 20° could be produced.

To examine how trajectory variations might be produced in the real frog, we performed a sensitivity analysis in which the torque pattern for maximal-distance jumping was systematically varied and used to drive the forward dynamics of model 4. Individual torque components forming the pattern were scaled in amplitude while the other torques were unaltered. We found that the take-off angle was most sensitive to variations in the amplitude of the hip external rotation torque (Fig. 11). Variations in torque by a factor of ±0.20 produced a 35° range of take-off angles, with increases in the torque magnitude leading to increases in the take-off angle. We also found that when the hip external rotation and knee extensor torque were varied simultaneously by a factor of only ±0.10, a 35° range of take-off angles could be produced. Interestingly, the cruralis, gluteus magnus and tensor fascia latae all externally rotate the hip and extend the knee and are activated during jumping (Peters et al., 1996; Gillis and Biewener, 2000). Thus, these muscles represent target muscles by which small variations in activation level might lead to large changes in take-off angle. We found that the horizontal take-off velocity, which probably determines in large part the success of escape jumps (Gans and Parsons, 1966; Howell, 1944), was most sensitive to variations in the amplitude of the hip extensor torque (see Fig. 11). Thus, the semimembranosus, gracilis and the dorsal head of the adductor magnus, which are the three primary hip extensor muscles in the frog, represent target muscles for controlling jump speed and distance (see Olson and Marsh, 1998).

Limitations of forward dynamic simulation; future modeling

Although forward dynamic simulations have proved to be a very useful tool to elucidate the role of various joint DOFs in jumping performance, this approach has several limitations. First, for computational simplicity, in most of the simulations we assumed: (i) that the torques around different joints were generated simultaneously, and (ii) that the torques were generated instantaneously and remained constant throughout the movement (i.e. torque steps). That torque generation is simultaneous seems to be supported by actual measurements (see Fig. 1), but the torques generated were neither instantaneous nor constant. Nonetheless, by running the models through the actual torques measured during jumping, we were able to show that these assumptions did not affect our general conclusions. As might be expected, a constant torque during the simulation tended to result in somewhat improved jumping. Thus, our findings of reduced performance in models with fewer joint DOFs are a manifestation of kinematic constraints rather than an 'unnatural' torque pattern.

A third limitation when discussing motor control is our assumption that individual torques can be independently manipulated. During maximal muscle recruitment and activation, this may not be true because most of the hindlimb muscles are biarticular and, hence, torques will necessarily be coupled at adjacent joints. During submaximal recruitment or activation, however, individual regulation of torques is probably possible by differential recruitment (or activation) of the muscles. Hence, the various levels of control of the take-off angle with the different models are probably possible during submaximal movements.

We believe that considerable improvements in modeling, and hence our understanding of skeletal design, can be

achieved by driving the skeleton with physiologically realistic muscle–tendon actuators rather than joint torque inputs. In this case, the observed rise in torque generation at the beginning of the jump will probably be well represented by two important mechanisms built into the actuator: the rate of muscle force generation and tendon compliance. Further, the drop in torque that occurs later in the jump will probably be closely represented by two other important mechanisms: the force/velocity properties of the muscle and the change in moment arm with joint position. Finally, activation of a biarticular muscle will lead to moments around both joints, thus providing a realistic evaluation of the amount of coupling of torque generation around adjacent joints.

In summary, our modular approach to examining the role of joint DOFs during jumping has provided insight into the role of the skeleton during frog jumping. This approach also provided some insight into neuromuscular mechanisms to control take-off angle and acceleration. These mechanisms will be further addressed in future studies by embedding musculotendon actuators and neural control within the skeletal framework developed here.

References

Alexander, R. McN. (1993). Optimization of structure and movement of the legs of animals. *J. Biomech.* **26 (Suppl. 1)**, 1–6.

Alexander, R. McN. (1995). Leg design and jumping technique for humans, other vertebrates and insects. *Phil. Trans. R. Soc. Lond. B* **347**, 235–248.

Blob, R. W. and Biewener, A. A. (2001). Mechanics of limb bone loading during terrestrial locomotion in the green iguana (*Iguana iguana*) and American alligator (*Alligator mississippiensis*). *J. Exp. Biol.* **204**, 1099–1122.

Calow, L. F. and Alexander, R. McN. (1973). A mechanical analysis of the hindleg of a frog (*Rana temporaria*). *J. Zool., Lond.* **171**, 293–321.

Crago, P. (2000). Creating neuromusculoskeletal models. In *Biomechanics and Neural Control of Posture and Movement* (ed. P. Crago and J. M. Winters), pp. 119–133. New York: Springer-Verlag.

Dhaherlab, Y. Y., Delp, S. L. and Rymer, W. Z. (2000). The use of basis functions in modeling joint articular surfaces: Application to the knee joint. *J. Biomech.* **33**, 901–907.

Emerson, S. B. (1978). Allometry and jumping in frogs: Helping the twain to meet. *Evolution* **32**, 551–564.

Emerson, S. B. and de Jongh, H. J. (1980). Muscle activity at the ilio-sacral articulation of frogs. *J. Morphol.* **166**, 129–144.

Fukson, O. I., Berkinblit, M. B. and Feldman, A. G. (1980). The spinal frog takes into account the scheme of its body during the wiping reflex. *Science* **209**, 1261–1263.

Gans, C. and Parsons, T. S. (1966). On the origin of the jumping mechanism in frogs. *Evolution* **20**, 92–99.

Gillis, G. B. and Biewener, A. A. (2000). Extensor muscle function during jumping and swimming in the toad (*Bufo marinus*). *J. Exp. Biol.* **203**, 3547–3563.

Giszter, S. F., McIntyre, J. and Bizzi, E. (1989). Kinematic strategies and sensorimotor transformations in the wiping movements of frogs. *J. Neurophysiol.* **62**, 750–767.

Hirano, M. and Rome, L. C. (1984). Jumping performance of frogs (*Rana pipiens*) as a function of muscle temperature. *J. Exp. Biol.* **108**, 429–439.

Howell, A. B. (1944). *Speed in Animals – Their Specialization for Running and Leaping.* Chicago, IL: Chicago University Press.

Kinzel, G. L. and Gutkowski, L. J. (1983). Joint models, degrees of freedom and anatomical motion measurement. *J. Biomech. Eng.* **105**, 55–62.

Lieber, R. L. and Boakes, J. L. (1988). Muscle force and moment arm contributions to torque production in frog hindlimb. *Am. J. Physiol.* **254**, C769–C772.

Lieber, R. L. and Shoemaker, S. D. (1992). Muscle, joint and tendon contributions to the torque profile of frog hip joint. *Am. J. Physiol.* **263**, R586–R590.

Lombard, W. P. and Abbot, F. M. (1906). The mechanical effects produced by the contraction of individual muscles of the thigh of the frog. *Am. J. Physiol.* **10**, 1–60.

Lutz, G. J., Bremner, S., Lajevardi, N., Lieber, R. L. and Rome, L. C. (1998). Quantitative analysis of muscle fiber type and myosin heavy chain distribution in the frog hindlimb: implications for locomotory design. *J. Muscle Res. Cell Motil.* **19**, 717–731.

Lutz, G. J. and Rome, L. C. (1994). Built for jumping: The design of the frog muscular system. *Science* **263**, 370–372.

Lutz, G. J. and Rome, L. C. (1996a). Muscle function during jumping in frogs. I. Sarcomere length change, EMG pattern and jumping performance. *Am. J. Physiol.* **271**, C563–C570.

Lutz, G. J. and Rome, L. C. (1996b). Muscle function during jumping in frogs. II. Mechanical properties of muscle: Implications for system design. *Am. J. Physiol.* **271**, C571–C578.

Mai, M. T. and Lieber, R. L. (1990). A model of semitendinosus muscle sarcomere length, knee and hip joint interactions in the frog hindlimb. *J. Biomech.* **23**, 271–279.

Marsh, R. L. (1994). Jumping ability of anuran amphibians. In *Advances in Veterinary Science and Comparative Medicine*, vol. 36B, *Comparative Vertebrate Exercise Physiology* (ed. J. H. Jones), pp. 51–111. New York: Academic Press.

Marsh, R. L. and John-Alder, H. B. (1994). Jumping performance of hylid frogs measured with high-speed cine films. *J. Exp. Biol.* **188**, 131–141.

Nigg, B. M. (1999). Measurement techniques. In *Biomechanics of the Musculoskeletal System*. Second edition (ed. B. M. Nigg and W. Herzog), pp. 350–399. New York: Wiley.

Olson, J. M. and Marsh, R. L. (1998). Activation patterns and length changes in hindlimb muscles of the bullfrog (*Rana catesbeiana*) during jumping. *J. Exp. Biol.* **201**, 2763–2777.

Pandy, M. G. and Sasaki, K. (1998). A three-dimensional musculoskeletal model of the human knee joint. Part 2. Analysis of ligament function. *Comput. Meth. Biomech. Biomed. Eng.* **1**, 265–283.

Peplowski, M. M. and Marsh, R. L. (1997). Work and power output in the hindlimb muscles of Cuban tree frogs *Osteopilus septentrionalis* during jumping. *J. Exp. Biol.* **200**, 2861–2870.

Peters, S. E., Kamel, L. T. and Bashor, D. P. (1996). Hopping and swimming in the leopard frog, *Rana pipiens*. I. Step cycles and kinematics. *J. Morphol.* **230**, 1–16.

Rome, L. C. and Lindstedt, S. L. (1997). Mechanical and metabolic design of the muscular system in vertebrates. In *Handbook of Physiology. Comparative Physiology*, section 13, vol. 1, chapter 23 (ed. W. H. Dantzler), pp. 1587–1651. Bethesda, MD: American Physiological Society.

Rome, L. C. and Lindstedt, S. L. (1998). The quest for speed: Muscles built for high-frequency contractions. *News Physiol. Sci.* **13**, 261–268.

Rome, L. C., Loughna, P. T. and Goldspink, G. (1984). Muscle fiber activity in carp as a function of swimming speed and muscle temperature. *Am. J. Physiol.* **247**, R272–R279.

Savazzi, E. (1999). Introduction to functional morphology. In *Functional Morphology of Invertebrates* (ed. E. Savazzi), pp. 1–23. New York: John Wiley & Sons Inc.

Tsai, L. W. (1999). Statics and stiffness analysis. In *Robot Analysis and Design: The Mechanics of Serial and Parallel Manipulators* (ed. L. W. Tsai), pp. 152–178. New York: John Wiley & Sons.

Vaughan, C. L., Davis, B. L. and O'Connor, J. C. (1996). *Dynamics of Human Gait*. Champaign, IL: Human Kinetics Publishers.

Yeadon, M. R. (1990). The simulation of aerial movement. II. A mathematical inertia model of the human body. *J. Biomech.* **23**, 67–74.

Zajac, F. E. (1993). Muscle coordination of movement: a perspective. *J. Biomech.* **26 (Suppl. 1)**, 109–124.